Title: A Comparative Study of Solute Trapping in Fe - (33-45 at.%) Cu Alloys Manufactured by Laser Directed Energy Deposition

Author list: Daniel Yin[a], Amit Misra[b]

Author Affiliation list:

[a] Graduate Student, Department of Materials Science and Engineering, University of Michigan, Ann Arbor, MI, 48109, USA

[b] Professor, Department of Materials Science and Engineering, University of Michigan, Ann Arbor, MI, 48109, USA

Author contributions:

1) Investigation, Methodology, Visualization, Analysis, Writing (original draft).
2) Supervision, Writing (review and editing).

Corresponding Author: Daniel Yin – dbyin@umich.edu

Keywords: directed energy deposition, Cu, Fe, modeling, phase equilibria

Declarations:

Funding: This project was supported by the Department of Energy, National Nuclear Security Administration under Award no. DE-NA0003857.

Conflicts of interest: The authors have no conflicts of interest to disclose.

Abstract:

The high cooling rates in laser directed energy deposition (DED-LB) of alloys lead to substantial amounts of solute trapping as solute atoms cannot diffuse away from the solid/liquid interface before it advances. In some concentrated alloys, this results in supersaturated solid phases that form nanoscale hierarchical microstructures when the solute atoms precipitate out during reheating from subsequent laser passes. We choose the Iron-Copper (Fe-Cu) binary alloy as model system as it is chemically homogeneous in the liquid phase and has negligible solid solubility at room temperature. Two alloys with nominal compositions in atomic (at.) %, $Fe_{67}Cu_{33}$ and $Fe_{55}Cu_{45}$, were manufactured using DED-LB. Scanning transmission electron microscopy (STEM), energy dispersive spectroscopy (EDS) and wavelength dispersive spectroscopy (WDS) were used to characterize the nanostructures and heterogeneous chemical compositions. A non-equilibrium solute partitioning model was used to compute the supersaturated chemistries of the constituent phases and validated with experimentally measured compositions. The measured phase compositions of the two alloys were very similar, at roughly 12 at.% Cu and 4 at.% Fe in the α(bcc)-Fe and ε(fcc)-Cu phases respectively, despite having different processing parameters and mechanical behavior. This indicates that the total thermal history, that depends on both the processing parameters and laser scan pattern, plays a stronger role on the final microstructure evolution than just the initial quantity of trapped solute. Additionally, we find that current non-equilibrium solute partitioning models applied on the continuum scale fall short of predicting accurate quantitative phase compositions in concentrated alloys, although the qualitative trends are captured correctly.

1) Introduction:

Laser directed energy deposition (DED-LB) is an additive manufacturing process that flows a metal powder stream into a laser beam where it is melted and deposited onto a substrate. It slots alongside laser powder bed fusion (PBF-LB) and wire fed arc directed energy deposition (DED-Arc) as well known and used additive manufacturing techniques. It usually trails the surface finish quality of PBF-LB and the build rate of DED-Arc. However, DED-LB has the advantage of flexibility in composition variation where the input powder composition can be controlled in-situ via multiple hoppers containing elemental powders. This contrasts with PBF-LB and DED-Arc where the entire build will generally be of a single composition using alloyed powder or drawn wire. As such, DED-LB is ideal for exploring new alloys and their solidification behavior under high cooling rate.

The Iron-Copper (Fe-Cu) binary is one such material system of interest as the different equilibrium crystal structures of Cu and Fe at room temperature results in negligible solid solubility. Indeed, solubility of Cu in the Fe-rich phase is only moderate when Fe is in its austenite phase γ(fcc)-Fe at elevated temperatures where it has the same crystal structure as Cu. Above the melting point, Cu and Fe form a chemically homogenous liquid while below, the poor solubility presents itself with the long and flat liquidus curve of the γ(fcc)-Fe + Liquid two phase region of the equilibrium binary phase diagram [1].

This changes of course under high cooling rates or undercooling amounts where solute trapping occurs during solidification. The γ(fcc)-Fe phase will solidify first and at the solid liquid interface, not all solute Cu atoms can diffuse away before the interface advances and traps them within γ(fcc)-Fe. As solid diffusion rates are orders of magnitude lower than that of liquid, back diffusion is minimal during the first laser pass yielding a non-equilibrium solidus α(bcc)-Fe phase. Meanwhile, the liquid phase is depleted of the equilibrium expected concentration of Cu and when cooled enough, will solidify into a non-equilibrium "liquidus" ε(fcc)-Cu phase.

This phenomenon in the Cu-Fe system has been explored numerously in the past with water cooled molds, laser surface remelting, and droplet experiments. Munitz [2] explored the effect of cooling rates on the microstructure of several Cu-Fe alloys ranging from 27.4 to 77.9 at.% Cu using water cooled copper plates and electron beam powder bed fusion (PBF-EB). He found that for alloys with Cu concentrations near equimolar, a columnar microstructure will form for cooling rates below 10^2 K/s while cooling rates from 10^4 to 10^6 K/s will yield dense Fe spheroidal morphologies indicative of a liquid phase spinodal decomposition prior to solidification. While in-depth composition analysis was not done, Munitz briefly mentioned that that the PBF-EB samples had Fe spheroids with Cu solute concentrations near 32.1 at.% Cu. This is far above the 7.6 at.% equilibrium solubility limit for Cu in γ(fcc)-Fe at the 1367 K peritectic [1].

Liu *et al.* [3] tested the effect of cooling rates on the solidification behavior of an Fe20Cu80 alloy using both graphite and copper molds. The microstructure they found was remarkably similar to that of Munitz with smaller Fe spheroids as expected due to the higher Cu concentration. They also performed energy dispersive spectroscopy (EDS) characterization of the larger Fe spherulites and found around 26.4 at.% Cu within indicating high amounts of solute trapping.

Lu *et al.* [4] explored the effect of undercooling an Fe50Cu50 alloy using both glass fluxing and container-less drop tube atomization. They found that their samples had undercoolings large enough to breech the spinodal decomposition curve alloying for liquid-liquid phase separation to occur. Similar to the previous authors, they found that the Fe-rich liquid phase solidified first into spherulites and that these spherulites had Cu solute concentrations around 32.1 at.%. Additionally, the authors measured Fe solute concentrations in the Cu matrix and found it to be much lower at 3.53 at.% for the glass fluxed sample and 9.8 at.% for the drop tube sample. They attributed the difference to the higher cooling rates of the drop tube sample. This seems to imply that the Cu solute concentration in the Fe phase which solidifies first is less dependent on cooling rate to reach a maximum compared to solute trapping of Fe in the Cu phase.

The aforementioned experiments took advantage of small interaction volume [2] or small material quantity [3, 4] to achieve solidification rates high enough to approach the theoretical limit of Cu solubility in the Fe rich phase predicted by Turchanin & Agraval [5]. This thermodynamic theoretical limit comes from the intersection of the T_0 curve with the spinodal curve that extends deeply into the γ(fcc)-Fe + Liquid two phase region. Here, T_0 represents the temperature for a given composition where the free energy curves of the solid and liquid phase intersect.

Indeed, to surpass this thermodynamic limit would require much high cooling rates. Cui *et al.* [6] ran MD simulations for the solidification of a Fe75Cu25 alloy and found that cooling rates on the order of 10^{12} K/s were needed to achieve amorphous solidification. In that case, the kinetic freezing of atoms in place is analogous to partition-free solidification and is different from partitionless crystalline solidification defined by Turchanin & Agraval [5] which is a thermodynamic process dependent on undercooling below T_0.

Recently, work by Chatterjee *et al.* [7] and Zafari *et al.* [8,9] showed that significant improvement in mechanical strength is achievable within Cu-Fe alloys manufactured by DED-LB and PBF-LB respectively due to Cu and Fe nanoprecipitate formation. However, neither work focused on characterizing the phase compositions which were supersaturated non-equilibrium prior to precipitating out during the reheating and remelting conditions of subsequent laser passes. As such, there has not been a significant effort to correlate the degree of non-equilibrium partitioning to the laser-additive processing parameters nor the powder composition chosen. The degree of non-equilibrium partitioning will relate directly to the resultant quantity of precipitates which contributes greatly to the improved strength of the alloys, often multiple times greater than the Hall-Petch predicted strength.

In this work, a comprehensive melt-pool and laser powder interaction model is applied to solve for the non-equilibrium phase compositions that form in two DED-LB manufactured concentrated Fe-Cu binary alloys. For the melt pool, governing equations of heat, fluid flow, and species transport are solved numerically in a manner similar to that of prior work by He *et al.* [10] and Qi *et al.* [11]. The laser powder interaction is solved in a semi-analytical manner with geometric assumptions regarding the powder flow trajectories. The laser intensity is not assumed to be Gaussian but follows a super-Gaussian formulation developed by Wu *et al.* [12,13]. Meanwhile, the coaxial annular powder concentration solution framework was built upon prior work on modeling powder nozzles by Lin [14], Pinkerton [15], Pinkerton *et al.* [16], and Wang *et al.* [17]. Together, the melt-pool transport model and the laser-powder interaction model allow us to simulate the DED-LB process.

A concentrated non-equilibrium solute partitioning model developed in a prior work, Yin *et al.* [18], is applied to solve for the non-equilibrium chemical compositions of the Fe-rich and Cu-rich phases that form as the homogeneous liquid cools through the γ(fcc)-Fe + liquid two-phase region. This non-equilibrium model is coupled with the aforementioned DED-LB model and thus, the non-equilibrium phase compositions can be solved and tracked for any node within the deposited track experiencing solidification.

The prior work [18] was mainly a theoretical study and compared our non-equilibrium solute partitioning model against similar models by other authors. One simulation was run with DED-LB processing parameters of the Fe55Cu45 alloy but severely overpredicted track height and non-equilibrium phase compositions. This is understandable as the old laser powder interaction model did not accurately predict the laser attenuation nor the powder stream broadening profile across the nozzle standoff distance. The old model assumed an ideal Gaussian beam with no defocus and a perfectly Gaussian powder stream profile with no broadening. And since the non-equilibrium model is sensitive to the melt-pool conditions, its accuracy is directly dependent on the energy balance and mass addition at the free surface calculated by the laser powder interaction model.

Finally, experimental samples produced by Chatterjee *et al.* [7] were sectioned and had their phase fraction and compositions characterized. Both the overall bulk composition as well as the compositions of the individual phases were mapped using wavelength dispersive spectroscopy (WDS) and scanning transmission electron microscopy–energy dispersive spectroscopy (STEM-EDS) respectively. Phase fraction analysis was done with ImageJ on backscattered electron (BSE) images taken from the same composition mapped regions. These characterization results are then compared with the modeled non-equilibrium phase compositions along with prior work by Lu *et al.* [4]. A thorough analysis of both our non-equilibrium partitioning model as well as Aziz's continuous growth model [19] is performed to explore the cause of deviations between predicted non-equilibrium phase compositions and their corresponding measured values.

Table 1 Variables used in the transport and non-equilibrium partitioning model

Nomenclature

Latin Symbols			
a	solute atom diameter (m)	k_{eq}	equilibrium partition coefficient
A_{ncs}	node cross-sectional area (m^2)	k_{ne}	non-equilibrium partition coefficient
b	solvent atom diameter (m)	K_0	Darcy coefficient
C	composition (wt%)	L	smoothing thickness factor (m)
C_l	liquidus composition (wt%)	$\bar{L}_m$	mass averaged latent heat of melting (J/kg)
$C_{l_{eq}}$	equilibrium liquidus compositions (wt%)	$\mathcal{L}$	latent energy term (J/kg)
$C_{l_{ne}}$	non-equilibrium liquidus composition (wt%)	$\boldsymbol{n}^*$	normal vector to free surface
C_s	solidus composition (wt%)	P	pressure (Pa)
$C_{s_{eq}}$	equilibrium solidus composition (wt%)	v_i	interface velocity (m/s)
$C_{s_{ne}}$	non-equilibrium solidus composition (wt%)	$\boldsymbol{V}$	fluid velocity (m/s)
C_P	powder composition (wt%)	$\boldsymbol{V_s}$	laser scan velocity (m/s)
$\bar{C}_p$	mass averaged heat capacity (J/(kg*K))	t	time (s)
$\bar{C}_{pl}$	mass averaged liquid heat capacity (J/(kg*K))	T	temperature (K)
$\bar{C}_{ps}$	mass averaged solid heat capacity (J/(kg*K))	T_i	ambient temperature (K)
d	level-set height	T_m	melting temperature (K)
D	diffusion coefficient (m^2/s)	u	x-component fluid velocity (m/s)
D_{ab}	interdiffusion coefficient (m^2/s)	u_s	laser scan velocity, x-component (m/s)
e_x	unit vector in x-axis	$\boldsymbol{u}$	fluid velocity, x-component (m/s)
f_l	liquid mass fraction (%)	W	weight fraction (%)
$f_{l_{eq}}$	equilibrium liquidus phase fraction (%)		
$f_{l_{ne}}$	non-equilibrium liquidus phase fraction (%)	***Greek Symbols***	
f_s	solid mass fraction (%)	β	dimensionless solidification rate
$f_{s_{eq}}$	equilibrium solidus phase fraction (%)	ε	emissivity
$f_{s_{ne}}$	non-equilibrium solidus phase fraction (%)	κ	curvature
F_{lv}	overall force function (m/s)	μ_l	dynamic viscosity ((N*s)/m^2)
F_p	powder force function (m/s)	ρ	density (kg/m^3)
g_x	standard gravity, x-component (m/s^2)	ρ_l	liquid density (kg/m^3)
g_l	liquid volume fraction (%)	ρ_s	solid density (kg/m^3)
h_c	heat transfer coefficient (W/(m^2*K))	σ	surface tension (N/m)
H	smoothing layer function	σ_b	Boltzmann constant (J/K)
k	thermal conductivity (W/(m*K))	φ	level-set (m)
${k_m}^*$	modified equilibrium partition coefficient	ϕ	arbitrary physical property

2) Description of Models:

2.1) Transport Model

A finite difference scheme is used to solve the transport model equations of heat, momentum, and species within the domain. For this model, we utilize a similar set of assumptions as in our prior work Yin *et al.* [18]. However, the introduction of a new laser-powder interaction model eliminates the assumptions of beam profile, powder heating, and powder concentration. The assumptions that remain are as follows:

1. The fluid flow in the melt pool is Newtonian, laminar, and incompressible.
2. Heat and mass loss from boiling in the melt pool are neglected.
3. The solid/liquid two-phase region is a porous medium with isotropic permeability.

The rationale for the assumptions is explained in detail within our prior work [18] and is omitted here for brevity. All the variables used in defining the transport model are listed in Table 1; the DED-LB processing parameters used are listed in Table 3.

2.1.1) Governing Equations

The implementation of the governing equations closely follows that of our prior work [18] with modifications to the condensed/gas phase interface boundary conditions due to the new laser-powder interaction model.

The conservation of mass is given by Eq. (1).

$$\frac{d\rho}{dt} + \nabla \cdot (\rho \boldsymbol{V}) = 0 \tag{1}$$

In the heat Eq. (2), $\mathcal{L}$ is the latent energy term. The solid/liquid source term $S^T_{S/L}$ [Eq. (3)] represents Stefan's condition which accounts for latent heat from phase change along a moving interface [20].

$$\begin{aligned}\frac{d(\rho \bar{C}_p T)}{dt} + \nabla\left(\rho \boldsymbol{V} \bar{C}_p T\right) = k\nabla^2 T - \nabla \cdot \left[\rho \boldsymbol{V} f_s (\bar{C}_{pl} - \bar{C}_{ps}) T\right] \\ - \nabla(\rho \boldsymbol{V} \mathcal{L}) + \nabla(\rho \boldsymbol{V}_s f_s \mathcal{L}) \\ + S^T_{S/L} + q_{L/G}\,\delta(\varphi)\end{aligned} \tag{2}$$

$$S^T_{S/L} = -\frac{d(\rho f_l \mathcal{L})}{dt} \tag{3}$$

$$\mathcal{L} = (\bar{C}_{ps} - \bar{C}_{pl})T_m + \bar{L}_m \tag{4}$$

The $q_{C/G}$ term encapsulates the energy input from the laser source (1030 nm disk laser), heated powder, as well as losses from convection and radiation [Eqs. (6)-(7)]. The $\delta(\varphi)$ term is a Dirac delta function of the level-set variable φ. It ensures that $q_{C/G}$ contributes to the heat Eq. (2) only at the free surface where $\varphi = 0$.

$$q_{C/G} = I_{att}A_{ncs} + E_{powder} - E_{loss} \tag{5}$$

$$E_{powder} = \begin{cases} F_{pd}\left[\rho_s\bar{C}_{ps}\left(T_{pd} - T_i\right)\right] & , \ T_{pd} < T_m \\ F_{pd}\left[\rho_s\bar{C}_{ps}(T_m - T_i)f_s + \rho_l\bar{L}_m f_l\right] & , \ T_{pd} = T_m \\ F_{pd}\left[\rho_s\bar{C}_{ps}(T_m - T_i) + \rho_l\left(\bar{L}_m + \bar{C}_{pl}\left(T_{pd} - T_m\right)\right)\right] & , \ T_{pd} > T_m \end{cases} \tag{6}$$

$$E_{loss} = h_c(T - T_i) - \sigma_b\varepsilon\left(T^4 - {T_i}^4\right) \tag{7}$$

The momentum equation for fluid flow and its boundary conditions are defined here for the x-axis [Eq. (8)]. The equations for the other two cartesian axes (*y, z*) are identical.

$$\frac{d(\rho u)}{dt} + \nabla\cdot(\rho\boldsymbol{u}u) = \nabla\cdot\left(\mu_l\frac{\rho}{\rho_l}\nabla\boldsymbol{u}\right) - \frac{dP}{dx} + S^u_{S/L} + S^u_{L/G} \tag{8}$$

The source term in the solid/liquid two-phase region $S^u_{S/L}$ [Eq. (9)], has two components. The left-side term is an implementation of Darcy's law for fluid flow retardation through a porous medium [21]. The right-side term is the body force caused by the temperature dependent density gradient. Since gravity has a non-zero value only in the z-axis, this term will not contribute to the source term in *x* and *y*.

$$S^u_{S/L} = -\frac{\mu_l}{K}\frac{\rho}{\rho_l}(u - u_s) - g_x\rho(T) \tag{9}$$

$$K = K_0\frac{{g_l}^3}{(1 - g_l)^2} \tag{10}$$

The source term at the liquid/gas interface $S^u_{L/G}$ [Eq. (11)], accounts for Marangoni flow caused by surface tension gradients at the free surface of the melt pool. These surface tension gradients are the result of high temperature gradients due to the focused laser beam.

$$S^u_{L/G} = \Big[-e_x\cdot\Big(\sigma\boldsymbol{n}^*\kappa - \nabla_S T\frac{d\sigma}{dT}\Big)\delta(\varphi)\Big)\Big] \tag{11}$$

The species governing Eq. (12) is defined in wt. %. Eq. (13) dictates that the boundary condition at the free surface of the melt pool and within the powder stream will be equal to the solved powder composition from the laser-powder interaction model.

$$\begin{aligned}\frac{d(\rho C)}{dt} + \nabla\cdot(\rho\boldsymbol{V}C) = {} & \nabla\cdot(\rho D\nabla C) + \nabla\cdot[\rho D\nabla(C_l - C)] \\ & -\nabla\cdot[\rho f_s(C_l - C_s)(\boldsymbol{V} - \boldsymbol{V_s})]\end{aligned} \tag{12}$$

$$C|_{\varphi=0} = C_P \tag{13}$$

2.1.2) Free Surface

The level-set method [Eq. (14)] is used to track the free surface evolution.

$$\varphi(x,y,z) = \pm d \tag{14}$$

Here, d is the distance from the free surface located at $d = 0$. Positive d values indicate positions above the free surface in the gas phase). Negative d values indicate positions below the free surface such as the substrate and deposited track. Multiple level-sets are calculated for small increments of d near $d = 0$ to track the change in the free surface from timestep to timestep using Eq. (15).

$$\frac{d\varphi}{dt} + F_{lv}|\nabla\varphi| = 0 \tag{15}$$

There is normally a large difference in thermophysical property values at the free surface between the gas and condensed phases. To ensure good convergence of the governing equations, a thin smoothing layer is used [Eq. (16)].

$$\phi_{gas} = \phi_{gas} + H\left(\phi_{condensed} - \phi_{gas}\right) \tag{16}$$

$$H = (0.5)^{\frac{\varphi}{L}} \tag{17}$$

2.1.3) Thermophysical Property Averaging

We use Kopp's law [22] to average the thermophysical property values using the overall composition calculated in Eq. (12).

$$\phi_{Cu-Fe} = \phi_{Cu}W_{Cu} + \phi_{Fe}W_{Fe} \tag{18}$$

ϕ_{Cu-Fe} represents the averaged value while ϕ_{Cu} and ϕ_{Fe} are the property values of the pure elements. W_{Cu} and W_{Fe} are the mass fractions in weight percent. Temperature dependent heat capacities are calculated using the Shomate equations for pure Cu and Fe in the NIST database [23]. Temperature dependent thermal conductivities are calculated from best fit curves using pure element data tabulated in a NSRDS-NBS volume [24]. Other thermophysical values used in the transport model are listed in Table 2.

Table 2 Physical and thermal properties of pure copper and pure iron

Property	**Copper**	**Iron**	**Units**
Solid Density	8960.0	7874.0	g/m^3
Liquid Density	8020.0	6980.0	g/m^3
Latent heat of Fusion	202300.0	247291.610	J/kg
Dynamic Viscosity	0.00403	0.0060	$(N*s)/m^2$
Thermal expansion coefficient	1.65E-6	11.8E-6	1/K
Surface tension at reference temperature	1.52	2.28	N/m
Surface tension thermal change	-0.00021	-0.00026	N/(m*K)

Table 3 DED-LB processing parameters used in transport model

Parameter	**Fe55Cu45**	**Fe67Cu33**	**Units**
Laser Power	500	900	W
Beam Radius	1.0	0.6	mm
Scanning Speed	6.0	6.3	mm/s
Powder Composition	50	50	at.% Fe
Powder Flow Rate	0.1	0.1	g/s
Powder Stream Radius	3.25	2.25	mm
Convective heat transfer coefficient	150.0	150.0	$W/(m^2*K)$
Emissivity	0.135	0.135	unitless
Ambient temperature	298	298	K

2.2) Non-Equilibrium Partitioning Model

The original non-equilibrium partitioning concentrated model [Eq. (19)] was developed by Kar and Mazumder [25]. That model was a single equation and represents an undetermined system when trying to solve for the two non-equilibrium phase compositions. Therefore, we couple Eq. (19) with a general mass conservation equation [Eq. (20)] based on the lever rule so that a unique solution to the pair of non-equilibrium phase compositions can be calculated [18].

$$k_{ne}{}^{n} = \frac{C_{s_{ne}}{}^{n}}{C_{l_{ne}}{}^{n}} = \frac{C_{s_{ne}}{}^{n-1}}{C_{l_{ne}}{}^{n}} + \frac{k_{m^*}{}^{n} + \beta^{n}}{1 + \beta^{n}}\left(1 - \frac{C_{l_{ne}}{}^{n-1}}{C_{l_{ne}}{}^{n}}\right) \tag{19}$$

$$f_{s_{ne}}{}^{n} * C_{s_{ne}}{}^{n} + f_{l_{ne}}{}^{n} C_{l_{ne}}{}^{n} = C_{overall}{}^{n} \tag{20}$$

Eq. (19)-(20) are defined in timestep format where the superscript *n* denotes the current timestep. Solving the system of equations [Eq. (19)-(20)] yields Eqs. (21)-(22) which are the current timestep non-equilibrium solidus and liquidus compositions respectively.

$$C_{s_{ne}}{}^{n} = \frac{\frac{k_{m^*}{}^{n} + \beta^{n}}{1 + \beta^{n}} C^{n} + f_{l_{ne}}{}^{n} \left(C_{s_{ne}}{}^{n-1} - \frac{k_{m^*}{}^{n} + \beta^{n}}{1 + \beta^{n}} C_{l_{ne}}{}^{n-1} \right)}{f_{l_{ne}}{}^{n} + \frac{k_{m^*}{}^{n} + \beta^{n}}{1 + \beta^{n}} f_{s_{ne}}{}^{n}} \tag{21}$$

$$C_{l_{ne}}{}^{n} = \frac{C^{n} - f_{s_{ne}}{}^{n} C_{s_{ne}}{}^{n}}{f_{l_{ne}}{}^{n}} \tag{22}$$

The non-equilibrium solidus and liquidus phase fractions used in Eqs. (20)-(22) are calculated using Eqs. (23)-(24). They are also a function of β such that when β becomes very large, their values become fixed.

$$f_{s_{ne}}{}^{n} = f_{s_{ne}}{}^{n-1} + \frac{1}{1 + \beta^{n}} \left(f_{s_{eq}}{}^{n} - f_{s_{ne}}{}^{n-1} \right) \tag{23}$$

$$f_{l_{ne}}{}^{n} = f_{l_{ne}}{}^{n-1} + \frac{1}{1 + \beta^{n}} \left(f_{l_{eq}}{}^{n} - f_{l_{ne}}{}^{n-1} \right) \tag{24}$$

For the first instance of solidification, (n = 0), Eq. (21)-(22) cannot be solved as $C_{s_{ne}}{}^{n-1}$ and $C_{l_{ne}}{}^{n-1}$ are not known. Therefore, the initial non-equilibrium solidus and liquidus phase compositions are approximated using Eqs. (25)-(26).

$$C_{s_{ne}}{}^{0} = C_{overall}{}^{-1} + \frac{1}{1 + \beta^{0}} \left(C_{s_{eq}}{}^{1} - C_{overall}{}^{-1} \right) \tag{25}$$

$$C_{l_{ne}}{}^{0} = C_{overall}{}^{-1} + \frac{1}{1 + \beta^{0}} \left(C_{l_{eq}}{}^{1} - C_{overall}{}^{-1} \right) \tag{26}$$

k_{m^*} is an “equilibrating” term that drives the non-equilibrium phase compositions solved by Eqs. (21)-(22) towards their respective equilibrium values when β approaches 0.

$$k_{m^*} = \frac{C_{s_{eq}}{}^{n} - C_{s_{eq}}{}^{n-1}}{C_{l_{eq}}{}^{n} - C_{l_{eq}}{}^{n-1}} \tag{27}$$

$$\beta = \frac{a^{2} |v_{i}{}^{n}|}{(a + b) D_{ab}{}^{n}} \tag{28}$$

β is the singular term that controls the degree of non-equilibrium partitioning and has a lower bound of 0 which represents equilibrium solidification conditions. Solving Eq. (21)-(22) at that lower bound will yield the equilibrium phase compositions. When β is very large, $C_{s_{ne}}{}^{n}$ and $C_{l_{ne}}{}^{n}$ become fixed to their respective values of the previous timestep.

Table 4 Variables used in the laser powder interaction model

Nomenclature

Latin Symbols

A_{cs}	powder cross-sectional area (m^2)
A_s	powder surface area (m^2)
Bi	Biot number
C_{pd}	powder composition (at%)
$\bar{C}_{p_{pd}}$	powder mass averaged heat capacity (J/(kg*K))
$C_{p_{shield}}$	shielding gas heat capacity (J/(kg*K))
d_{nl}	distance nozzle to focusing lens (m)
d_{ns}	distance nozzle to substrate (m)
f_{length}	focal length (m)
h	heat transfer coefficient (W/(m^{2}K))
I_{att}	attenuated laser intensity (W/m^2)
I_0	original laser intensity (W/m^2)
k_{coef}	super Gaussian order fitting coefficient
k_{pd}	powder thermal conductivity (W/(m*K))
k_{shield}	shielding gas thermal conductivity (W/(m*K))
k_{SG}	super Gaussian order
L_{pd}	powder latent heat term (J/s)
m_{pd}	powder particle mass (kg)
$\dot{m}_{pd}$	powder flow rate (kg/s)
P_0	laser power (W)
Pr	Prandtl number
Re	Reynolds number
r_{focal}	powder nozzle focal point radius (m)
R_{nbc}	powder nozzle center to beam center (m)
R_{noz}	current powder stream radius (m)
R_{noz_0}	initial powder stream radius (m)
r_{pd}	powder particle radius (m)
R_{SGB}	super Gaussian beam radius (m)
r_{stream}	focused powder stream radius (m)
sg_1	super Gaussian radius coefficient 1
sg_2	super Gaussian radius coefficient 2
T_{old}	previous powder temperature (K)
T_{pd}	current powder temperature (K)
T_s	shielding gas temperature (K)
v_{pd}	powder velocity (m/s)
v_{shield}	shielding gas velocity (m/s)
x_{beam}	laser beam center x coordinate (m)
x_{ht}	transformed node x coordinate (m)
x_{in}	input node x coordinate (m)
x_s	input node shifted x coordinate (m)
y_{beam}	laser beam center y coordinate (m)
y_{ht}	transformed node y coordinate (m)
y_{in}	input node y coordinate (m)
y_s	input node shifted y coordinate (m)
z_{df}	laser defocusing length (m)
z_{focal}	powder nozzle focal height (m)
z_{ht}	transformed node z coordinate (m)
z_{in}	input node z coordinate (m)
z_r	laser Rayleigh length (m)

Greek Symbols

α_{pd}	powder absorptivity (%)
Γ_{coef}	Super Gaussian fitting coefficient
ζ_b	boiling phase change parameter
ζ_m	melting phase change parameter
ε_{pd}	powder emissivity
θ	nozzle offset angle xy plane (rad)
μ_{shield}	shielding gas viscosity ((N*s)/m^2)
ρ_{shield}	shielding gas density (kg/m^3)
σ_b	Boltzmann constant (J/K)
ψ	powder stream angle (rad)
ω	powder stream broadening angle (rad)

2.3) Laser-Powder Interaction Model

A semi-analytical model is developed to simulate the powder stream of an annular powder nozzle. It calculates the powder number concentration, laser attenuation, and powder temperature used in the boundary conditions of the melt pool transport model. This laser powder interaction model operates under the following assumptions:

1. The powder particle velocity is constant
2. The powder particle trajectories are linear
3. The laser attenuation is proportional to the cross-sectional area of powder particles

The first assumption is reasonable given the short travel time of the powder before impacting the free surface. The effects of gravity and atmospheric drag will be negligible. Additionally, the low powder flow rate results in a small volume fraction of powder in flight which precludes the probability of inter-particle collisions. The second assumption allows us to formulate the linear projected powder path heating (LPPH) scheme used to calculate both the laser attenuation as well as powder temperature. The LPPH scheme dictates that any given node on the free surface has one linear powder path per powder stream that maps to each powder stream's focal point. In an annular powder nozzle, the powder stream is radially symmetric and can be decomposed into a 2D representation with two diametrically opposite powder streams.

In this model, the distance between the nozzle and the substrate d_{ns} in the z-axis is discretized. Starting at d_{ns}, we step down one z-step for each iteration and calculate each projected path's new xy position using the path's slope and then solve for the powder number concentration, laser attenuation and powder temperature. The powder number concentration is summed between the two streams based on superposition theory. The cross-sectional area is proportional to the number concentration and dictates the laser attenuation. Meanwhile the powder temperature is mass averaged depending on each stream's mass concentration.

Finally, if a linear powder path does not fall within the nozzle's powder tube radii at the nozzle height d_{ns}, then that powder path's powder stream will not contribute to the final averaged powder concentration and powder temperature.

The full list of variables used in the laser-powder interaction model are compiled in Table 4; the nozzle and beam parameter values are listed in Table 5.

2.3.1) Coordinate frame transformation:

First, the x_{in} and y_{in} coordinates of the free surface must be shifted to the reference frame of the laser beam position given by $x_{beam}(t)$ and $y_{beam}(t)$ where t is the current simulated time. In Eqs. (29)-(30), x_s and y_s represent the shifted coordinate inputs. This sets the laser beam center as the origin and simplifies the equations for both the powder number concentration and laser beam intensity. Our z_{in} input does not need to be shifted as it is independent of the beam's travel in the x and y axes.

$$x_s = x_{in} - x_{beam}(t) \tag{29}$$

$$y_s = y_{in} - y_{beam}(t) \tag{30}$$

Then, we define a homogeneous transformation matrix to convert from the coordinate frame $[xyz]$ of the laser beam to that of the powder nozzle $[x_p y_p z_p]$. The overall transformation matrix is the product of three sub-matrices. From left to right they are: a clockwise rotation about the y-axis by the powder stream angle ψ, a counterclockwise rotation about the z-axis by the powder nozzle's angle θ off of the positive x-axis, and a translation in the $[x_p y_p z_p]$ coordinate frame. For the translation sub-matrix, R_{nbc} is the distance from the nozzle to the laser beam center and d_{ns} is the distance from the nozzle to the substrate.

$$\begin{aligned}&\text{HT}_{\text{matrix}}\\ &= \begin{bmatrix} \cos(\psi) & 0 & -\sin(\psi) & 0 \\ 0 & 1 & 0 & 0 \\ \sin(\psi) & 0 & \cos(\psi) & 0 \\ 0 & 0 & 0 & 1 \end{bmatrix} \begin{bmatrix} \cos(\theta) & \sin(\theta) & 0 & 0 \\ -\sin(\theta) & \cos(\theta) & 0 & 0 \\ 0 & 0 & 1 & 0 \\ 0 & 0 & 0 & 1 \end{bmatrix} \begin{bmatrix} 1 & 0 & 0 & -R_{\text{nbc}}\cos(\theta) \\ 0 & 1 & 0 & -R_{\text{nbc}}\sin(\theta) \\ 0 & 0 & 1 & -d_{ns} \\ 0 & 0 & 0 & 1 \end{bmatrix}\end{aligned} \tag{31}$$

With the homogeneous transformation matrix Eq. (31), we can convert our input coordinates using Eq. (32).

$$\begin{bmatrix} x_{ht} \\ y_{ht} \\ z_{ht} \\ 1 \end{bmatrix} = \text{HT}_{\text{matrix}} \cdot \begin{bmatrix} x_s \\ y_s \\ z_{\text{in}} \\ 1 \end{bmatrix} \tag{32}$$

To represent the two powder streams of an annular powder nozzle, we use the convention that the node is at an angle θ off the positive x-axis. Then the first stream will be along angle θ while the second stream will be along the angle $(\theta + \pi)$. The powder stream angle ψ may be approximated from the internal geometry of the powder nozzle in use. In our DED-LB setup, we determine it to be approximately 9.8 degrees.

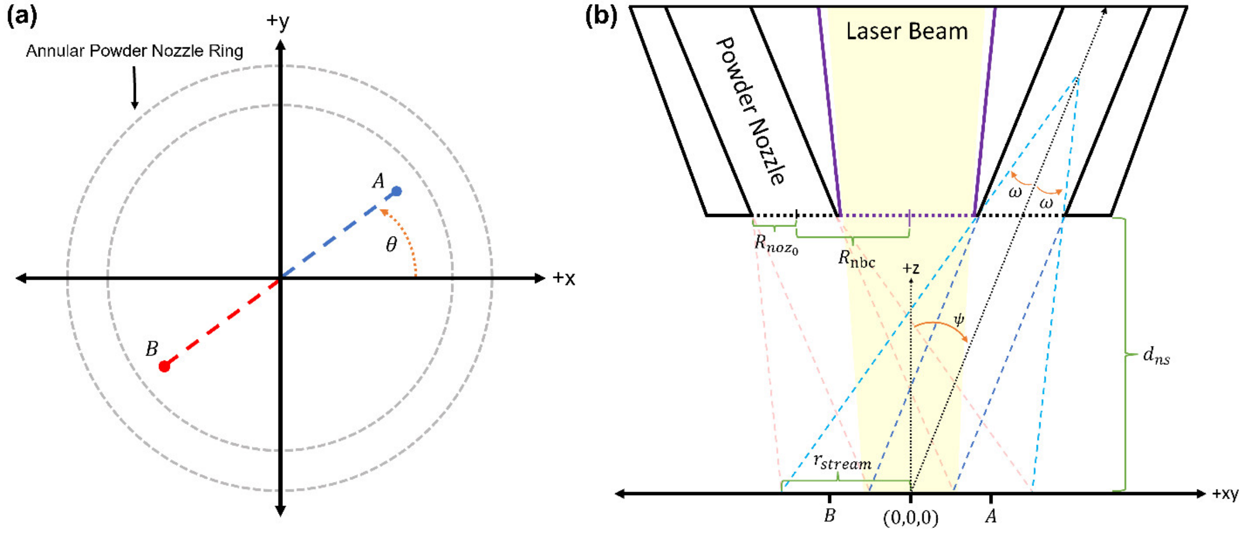

Figure 1. (a) The schematic shows how a node, A, on the free surface has a set of (x,y) coordinates which when projected on the xy plane at z = 0, will have an angle θ off of the positive x-axis. An equivalent and opposite angle

$\theta + \pi$ is also present based off a "mirrored" node B. Then there is a plane C, orthogonal to the xy plane, and along the line $\overleftrightarrow{AB}$ for which we will define our 2D representation of the powder streams of an annular powder nozzle **(b)** A schematic (*not drawn to scale*) of the two distinct powder streams on plane C. The angles and lengths of importance are labeled. Note that the two powder streams are radially symmetric about the laser beam center such that the labeled lengths and angles apply to both streams.

Table 5 Laser powder interaction model variable values

Variable	**Symbol**	**Value**	**Units**
Powder stream angle	ψ	9.8	degrees
Nozzle standoff distance	d_{ns}	20	mm
Nozzle center to beam center	R_{nbc}	3.425	mm
Initial powder stream radius	R_{noz_0}	0.925	mm
Focal length	f_{length}	270	mm
Distance nozzle to focusing lens	d_{nl}	150	mm
Laser Rayleigh length	z_r	8.95	mm
Focused Gaussian beam radius	R_{GB_0}	0.5	mm

2.3.2) Powder stream broadening angle

We must account for the powder stream broadening angle ω as powder streams will naturally expand upon leaving the nozzle. This angle is determined by first measuring both the powder nozzle opening half-width R_{noz_0} and the powder stream radius r_{stream} at the nozzle standoff distance d_{ns}. For the Fe55Cu45 and Fe67Cu33 cases, r_{stream} was 3.25 mm and 2.25 mm respectively. Then Eqs. (33)-(35) define the side-lengths of the complementary triangle formed underneath the radially expanding powder stream along the powder stream's z-axis z_p. Finally, Eq. (36) solves for ω where $\mathrm{adj_{pd}}$ is subtracted from $\mathrm{hyp_{pd}}$ to form an offset half isosceles triangle with known side-lengths.

$$\mathrm{hyp_{pd}} = \sqrt{{R_{\mathrm{nbc}}}^2 + {d_{ns}}^2} \tag{33}$$

$$\mathrm{adj_{pd}} = \cos\left(\frac{\pi}{2} - \psi\right)\left(r_{stream} - R_{noz_0}\right) \tag{34}$$

$$\mathrm{opp_{pd}} = \sin\left(\frac{\pi}{2} - \psi\right)\left(r_{stream} - R_{noz_0}\right) \tag{35}$$

$$\omega = \mathrm{atan}\left(\frac{\mathrm{opp_{pd}}}{\mathrm{hyp_{pd}} - \mathrm{adj_{pd}})}\right) \tag{36}$$

2.3.3) Powder Nozzle Focal Point

The calculated powder broadening angle ω then allows us to calculate the focal point of each powder stream. This focal point serves as the origin for which powder paths are linearly projected to all nodes on the free surface. In doing so, we identify which projected powder paths for a given node fall outside the powder tubes' radii. These projected paths will therefore be excluded. The final powder number concentration and powder temperature for each free surface node will be from its non-excluded paths, if any. Calculating the focal point involves another triangle construction [Eqs. (37)-(38)] and gives us the height z_{focal} and radius r_{focal} of the focal point. While r_{focal} is in the $[xyz]$ coordinate frame, z_{focal} is in the $[x_p y_p z_p]$ coordinate frame. It can be transformed to its corresponding $[xyz]$ coordinate frame value by multiplying with $\sin\left(\frac{\pi}{2}-\psi\right)$.

$$\text{adj}_{\text{focal}} = \frac{R_{noz_0}}{\tan(\omega)} \tag{37}$$

$$\text{opp}_{\text{focal}} = R_{noz_0}\tan(\psi) \tag{38}$$

$$z_{\text{focal}} = \text{adj}_{\text{focal}} + \text{opp}_{\text{focal}} + \text{hyp}_{\text{pd}} \tag{39}$$

$$r_{\text{focal}} = \sin(\psi)\, z_{\text{focal}} \tag{40}$$

Using the calculated powder stream focal point, we can calculate the slope $m(x,y)$ [Eq. (41)] from the node on the free surface and then check if the projected path falls within the powder tube radii using Eq. (42). In Eq. (41), the brackets $[x_s, y_s]$ indicate that we are solving for slope values in both the x and y directions. In Eq. (42), the vertical brackets represent taking the magnitude of the elements within.

$$m(x,y) = \frac{[r_{\text{focal}}\cos(\theta), r_{\text{focal}}\sin(\theta)] - [x_s, y_s]}{z_{\text{focal}}\sin\left(\frac{\pi}{2}-\psi\right) - z_{in}} \tag{41}$$

$$\left(R_{\text{nbc}} - R_{noz_0}\right) < \left|[x_s, y_s] + m(x,y)(d_{ns} - z_{in})\right| < \left(R_{\text{nbc}} + R_{noz_0}\right) \tag{42}$$

For each iteration where we step down one z-node, the slope $m(x,y)$ is used to calculate the updated coordinates of each projected powder path using the homogeneous transformation matrix Eq. (32). It should then be clear that at the last iteration where we are at the free surface z-node, both the input and transformed coordinates for all the nozzles will be the same and the powder concentration and laser attenuation equation will only need to be solved once. However, powder heating will still need to be solved separately as each powder path can experience unequal heating during their travel from the nozzle to the free surface. Only the node at the laser beam center $\left(x_{beam}(t), y_{beam}(t)\right)$ will have equal powder heating from all powder streams.

2.3.4) Powder number concentration

Using the calculated powder broadening angle ω, we can solve for the expanded powder stream radius R_{noz} [Eq. (43)] for each iteration's transformed z_{in} value, z_{ht}. Then, following the assumption that each individual stream's cross-section has a Gaussian profile in its $\left[x_p y_p z_p\right]$ coordinate frame along the z_p axis, our summed powder number concentration may be solved by Eq. (44). The presence of a summation is because each nozzles' streams can contribute to the powder concentration at a given point (x_{ht}, y_{ht}, z_{ht}) depending on whether the projected path from the node's free surface coordinates maps to within the powder tubes' radii. As such, n represents the number of projected paths that will be contributing to the powder number concentration.

$$R_{noz} = R_{noz_0} - z_{ht}\tan(\omega) \tag{43}$$

$$\mathrm{N}_{powder}(x_{ht}, y_{ht}, z_{ht}) = \sum_{i=0}^{n} \frac{2\dot{m}_{pd}}{m_{pd} v_{pd} \pi {R_{noz}}^2} \exp\left[-\frac{2({x_{ht}}^2 + {y_{ht}}^2)}{{R_{noz}}^2}\right] \tag{44}$$

2.3.5) Laser intensity

Instead of using the common approach of approximating the beam intensity as a pure Gaussian profile, we take the approach of Wu *et al.* [13] who characterized a fiber fed laser beam to more closely match that of a super-Gaussian profile. A super-Gaussian beam profile is similar to a top-hat profile or square wave but with a gentler slope instead of a sharp discrete drop at the beam radius.

We first calculate the defocusing length z_{df} given our focal length f_{length} of 270 mm. Then we solve for the super-Gaussian parameter k_{SG} with Eq. (46) where $k_{coef} = 0.04923$ and $\Gamma_{\text{coef}} = 3.174$. Then we solve for the super-Gaussian beam radius R_{SGB} using the measured focused beam radii R_{GB_0} of 0.5 mm. Here, the first super-gaussian coefficient $sg_1 = -2.519 * 10^{-17}$ and the second super-gaussian coefficient $sg_2 = 0.8936$. Finally, we solve for the unattenuated laser intensity I_0 [Eq. (48)] where Γ is the Gamma function.

$$z_{df} = f_{length} - z - (d_{ns} + d_{nl}) \tag{45}$$

$$k_{SG} = 1 + \frac{0.5\Gamma_{\text{coef}}}{k_{coef}\left({z_{df}}^2 + (0.5\Gamma_{\text{coef}})^2\right)} \tag{46}$$

$$R_{SGB} = R_{GB_0}\sqrt{1 + \left(\frac{z_{df}}{z_r}\right)^2} - sg_1 \exp\left[-\left(\frac{z_{df}}{sg_2}\right)^2\right] \tag{47}$$

$$\mathrm{I}_0(x_s, y_s, z) = \frac{2^{\frac{1}{k_{SG}}} k_{SG} P_0}{\pi R_{SGB}{}^2 \Gamma\left(\frac{1}{k_{SG}}\right)} \exp\left[-2\left(\frac{x_s{}^2 + y_s{}^2}{R_{SGB}{}^2}\right)^{k_{SG}}\right] \tag{48}$$

2.3.6) Laser attenuation

The beam attenuation is calculated using a laser attenuation scheme developed by Wang *et al.* [17] based on the powder/beam area obscuring ratio pd_{ratio}. This scheme calculates an effective powder number pd_{eff} [Eq. (51)] that describes the degree at which powder particles obscure the beam while accounting for powder particle overlap. This is dependent on the number of powder particles pd_{num} along the z-axis from the powder path's current z coordinate z_{in} up to the z-height of the nozzle d_{ns}.

$$pd_{ratio} = \frac{R_{SGB}{}^2}{pd_{rad}{}^2} \tag{49}$$

$$pd_{num} = \int_{z_{in}}^{d_{ns}} \frac{2\dot{m}_{pd}}{m_{pd} v_{pd}} \exp\left[-\frac{2(x_{ht}{}^2 + y_{ht}{}^2)}{R_{noz}{}^2}\right] dz \tag{50}$$

$$pd_{eff} = 1 - \left[\frac{pd_{ratio} - 1}{pd_{ratio}}\right]^{pd_{num}} \tag{51}$$

$$I_{att}(x_s, y_s, z) = \mathrm{I}_0(x_s, y_s, z) * pd_{eff} \tag{52}$$

The integral in Eq. (50) is done in the $[xyz]$ coordinate frame because the laser beam intensity is defined in that coordinate frame. When integrating along z, x and y are constant in $[xyz]$ but not in $[x_p y_p z_p]$, and so we must use the $\mathrm{HT}_{\mathrm{matrix}}$ to define Eq. (50) in terms of x, y, and z. As the integral in the modified Eq. (50) does not have an analytical form, we utilize an implementation of the tanh-sinh quadrature by van Engelen [26] to perform numerical integration.

2.3.7) Powder temperature

The powder temperature is calculated by the energy balance Eq. (56). We account for absorbed laser intensity, convective and radiative losses, as well as the latent energy from melting and boiling. The heat transfer coefficient of the powder in flight is calculated using Eqs. (53)-(55) which is an analytical relationship of the Reynolds and Prandtl number derived by Liu and Lin [27].

$$\mathrm{Re} = 2r_{pd}\rho_{shield}\left(\frac{v_{shield} - v_{pd}}{\mu_{shield}}\right) \tag{53}$$

$$\mathrm{Pr} = \frac{C_{p_{shield}} \mu_{shield}}{k_{shield}} \tag{54}$$

$$h = \frac{k_{shield}}{2r_{pd}}(2 + 0.6\mathrm{Re}^{0.5}\mathrm{Pr}^{0.33}) \tag{55}$$

$$m_{pd}\bar{C}_{pd}\frac{dT_{pd}}{dt} = \frac{1}{4}A_s\alpha_{pd}\mathrm{I}_{\mathrm{att}} - hA_s(T_{old} - T_s) - \sigma_b\varepsilon_{pd}A_s\left({T_{old}}^4 - {T_s}^4\right) - L_{pd} \tag{56}$$

$$L_{pd} = \zeta_m L_m\frac{dm_m}{dt} + \zeta_b L_b\frac{dm_b}{dt} \tag{57}$$

If the increase in temperature dT for a given timestep dt is large enough to shift the temperature past the melting or boiling points, the effect of the latent heats must be accounted for. In those cases, the excess energy that would normally increase the temperature now goes to partially transforming the particle. Only once the powder particle has fully transformed will the temperature increase past the phase transformation temperature. Eq. (57) represents the latent heat terms where ζ_m and ζ_b are logical parameters equal to 1 at their respective phase change temperature and 0 elsewhere.

3) Results and Discussion:

3.1) Modeling: Non-Equilibrium Phase Compositions

Two simulations were run with the parameters listed in **Table 3** to match experimental samples made by Chatterjee *et al.* [7]. The substrate was initialized to 99.99 at.% Fe to emulate a mild steel substrate and its carbon concentration was neglected for composition calculations. The laser beam scans along the x-axis for a single pass and the simulations were run to a real time of around 0.7 seconds putting the laser beam center at roughly x = 4.2 mm and x = 4.4 mm for the Fe55Cu45 and Fe67Cu33 cases, respectively.

Figure 2 shows the 2D cross-sectional plots of the non-equilibrium solidus and liquidus phase compositions for the Fe55Cu45 set of processing parameters. We note that there is an initial region of instability in the first two millimeters of deposited material as the melt pool shape has not yet developed into a steady state moving front. This results in a lower overall Fe concentration which affects the calculated non-equilibrium phase compositions due to its appearance in Eqs. (21)-(22). This initial instability in the overall composition profile is consistent with prior DED-LB simulations by Gan *et al.* [28] on a cobalt alloy steel.

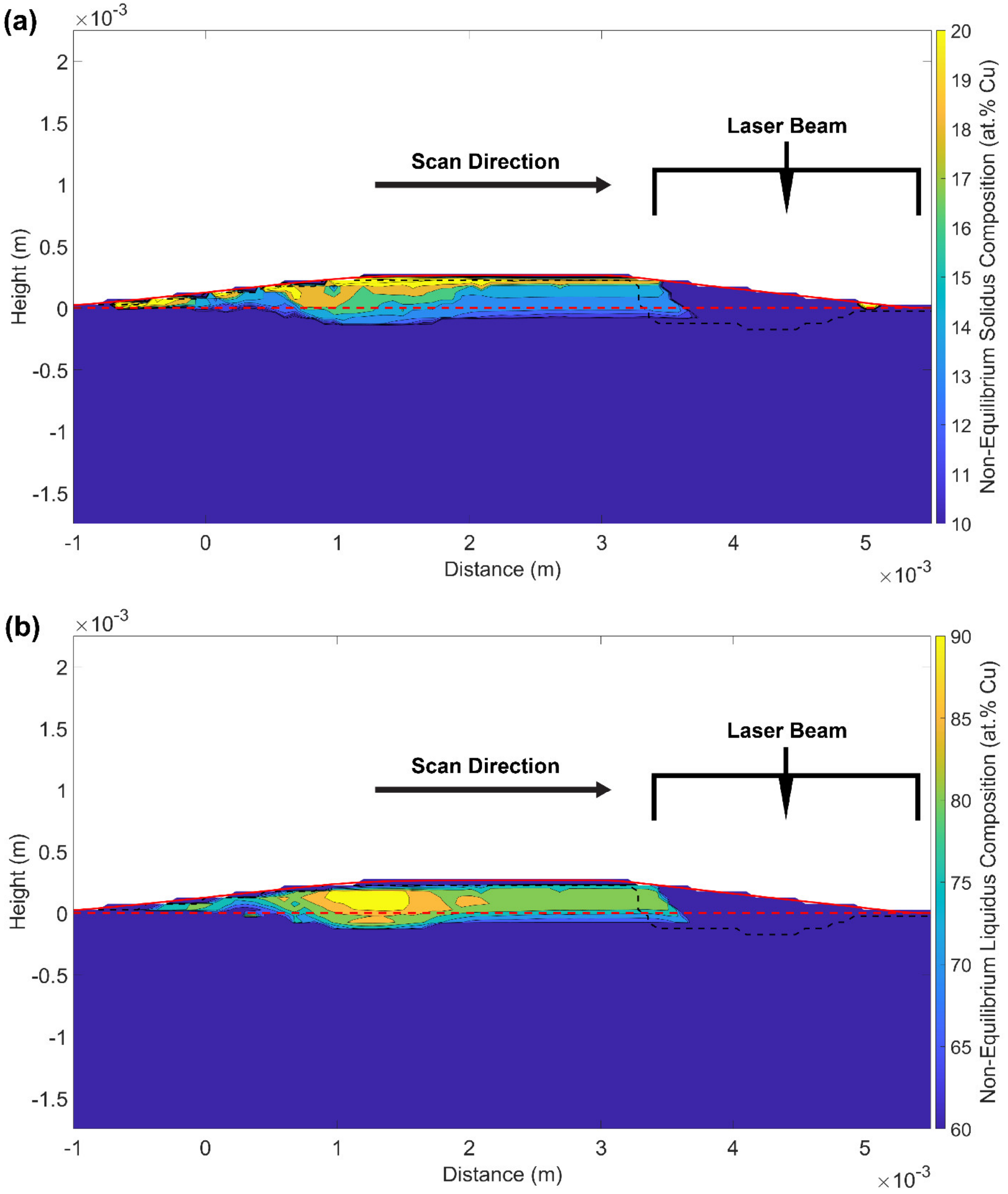

Figure 2. (a) A 2D cross-section plot of the non-equilibrium solidus phase compositions for a Fe55Cu45 simulation. Distance and height represent the x-axis and z-axis respectively. This plot depicts the xz plane at y = 3.659E-5 m. The solid red line indicates the free surface, the dashed red line indicates the original substrate height, and the dashed black line within the track and substrate indicates the melt-pool interface. The black bracket depicts the laser beam's cross-sectional coverage (0.6 mm radius) at the current timestep with the arrowhead representing the beam center. **(b)** A 2D cross-section plot of the non-equilibrium liquidus phase compositions. Non-equilibrium liquidus compositions outside the melt pool represent the solidified non-equilibrium ε(fcc)-Cu phase.

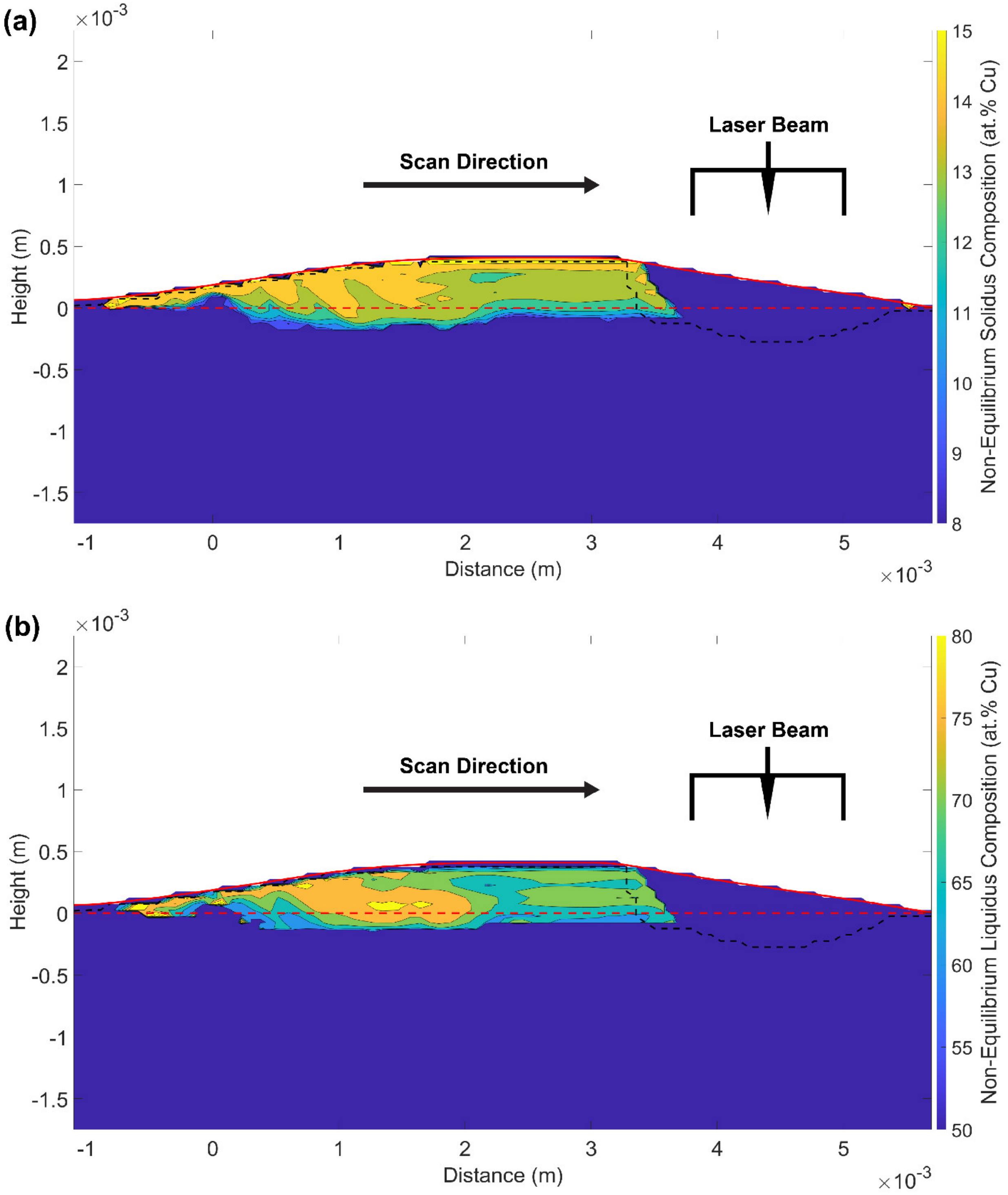

Figure 3. (a) A 2D cross-section plot of the non-equilibrium solidus phase compositions for a Fe67Cu33 simulation. Distance and height represent the x-axis and z-axis respectively. This plot depicts the xz plane at y = 3.659E-5 m. The solid red line indicates the free surface, the dashed red line indicates the original substrate height, and the dashed black line within the track and substrate indicates the melt-pool interface. The black bracket depicts the laser beam's cross-sectional coverage (0.6 mm radius) at the current timestep with the arrowhead representing the beam center. **(b)** A 2D cross-section plot of the non-equilibrium liquidus phase compositions. Non-equilibrium liquidus compositions outside the melt pool represent the solidified non-equilibrium ε(fcc)-Cu phase.

Figure 3 shows a similar pair of 2D cross-sectional plots for the Fe67Cu33 set of processing parameters. The same initial instability region is also present here as expected. Comparing the two processing parameter sets, we note the difference in track height at roughly 0.27 mm in the Fe55Cu45 case and 0.41 mm in the Fe67Cu33 case. This difference is largely due to the larger focal powder flow radius of 3.25 mm in the Fe55Cu45 case compared to 2.25 mm for Fe67Cu33.

The peak cooling rates of our simulations are around 20,000 K/s at the trailing end of the melt pool at the free surface. This falls within the expected range of cooling rates for DED-LB which ranges from 10^3 K/s to 10^5 K/s though the upper bound is generally more in the domain of PBF-LB [29]. For the Fe55Cu45 case, the non-equilibrium solidus and liquidus compositions at nodes just below the free surface in the steady state region past x = 2 mm are 14.9 at.% Cu and 83.3 at.% Cu respectively. For the Fe67Cu33 case, the corresponding non-equilibrium solidus and liquidus compositions are 14.3 at.% Cu and 74.3 at. % Cu respectively. We do not consider the nodes directly at the free surface as the shallow curvature of the melt-pool leads to nodes transitioning from being in the gas state to being incorporated into the track instantaneously. This leads to abnormally high initial values calculated by Eqs. (25)-(26) and skews the non-equilibrium phase compositions above their expected values. This skewed layer is most apparent in the plotted non-equilibrium solidus compositions in Figure 2(a) and Figure 3(a) as the smaller composition range c-axis highlights the surface layer.

The non-equilibrium solidus compositions in the Fe55Cu45 case have a very small gradient increasing towards the free surface. Nodes near the original substrate height have non-equilibrium solidus compositions around 13.5 at.% Cu which increases to the aforementioned 14.9 at.% Cu just under the free surface. This is expected as cooling rates increase towards the free surface. The Fe67Cu33 case has a similar gradient starting at roughly 12.5 at.% Cu near the original substrate height and increasing to 14.3 at.% Cu just under the free surface. However, a part of these non-equilibrium phase composition gradients is due to the overall composition gradient where Fe concentration increases down towards the substrate. This is due to the convective flow within the melt pool bringing substrate Fe species into the track and is expected for the initial deposition layers given how thin they are. Therefore, only nodes near the free surface have overall compositions close to the powder composition. Consequently, the non-equilibrium liquidus phase compositions have a reverse gradient where the Cu concentration decreases towards the substrate. Normally, we would correlate decreasing Cu concentration in the non-equilibrium liquidus as increased non-equilibrium partitioning due to higher cooling rates. However, cooling rates decrease towards the substrate and this gradient is due to the influence of the overall composition term in Eq. (22). As overall composition decreases, it causes a commensurate decrease in the non-equilibrium liquidus compositions.

3.2) Experiment: Composition Characterization

Cross-sectional cutouts of the DED-LB made samples were taken for polishing prior to composition mapping. The Fe55Cu45 sample was manufactured as a 1 cm cube with a 0.5 mm track overlap pattern. The Fe67Cu33 sample was manufactured as a 4-layer single track deposition 2 cm in length. Bulk composition mapping was done with wavelength dispersive spectroscopy (WDS) on a Cameca SX100. This quantification was done with calibrated pure Cu and Fe standards; it used a method described by Donovan *et al.* [30]. Figure 4(a) shows the composition map for the Fe55Cu45 sample while Figure 4(b) is the corresponding map for the

Fe67Cu33 sample. The overall composition was 55±2.5 at.% Fe for the Fe55Cu45 sample. Meanwhile the Fe67Cu33 sample had a bulk composition gradient ranging from 67±2.5 at.% Fe just above the substrate to 63±2.5 at.% Fe at the free surface.

Both samples used a starting powder composition of 50 at.% Fe which is not reflected in the measured overall composition. However, this is expected as our model's laser powder interaction solver predicts powder compositions at the free surface that match well with the measured overall compositions for both the Fe55Cu45 and Fe67Cu33 set of processing parameters. The difference between starting powder composition and resulting bulk composition is due to the preferential boiling of Cu powder with the Fe67Cu33 sample losing more Cu content due to the higher 900 W laser power.

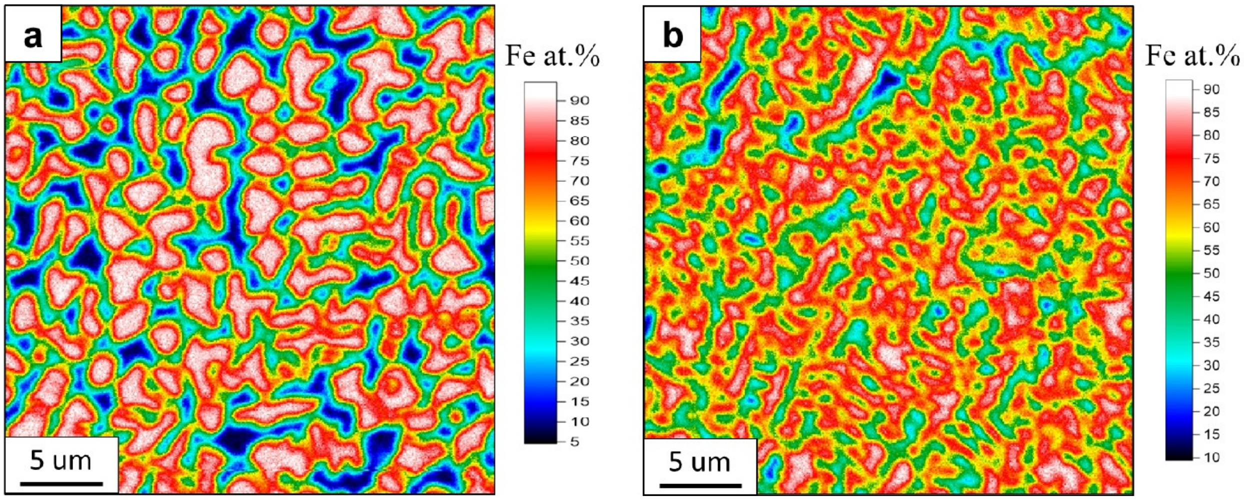

Figure 4. (a) WDS map of the Fe55Cu45 sample with large Fe grains visible in white and the Cu matrix in blue. The red speckles within the Fe grains represent the contribution from Cu nanoprecipitates. **(b)** A corresponding WDS map of the Fe67Cu33 sample also focused on the Fe grains. The higher Fe concentration and thinner dendrite spacing washes out the Cu matrix into a green shade.

Subsequently, focused ion beam (FIB) milled lift outs were taken from both the Fe55Cu45 and Fe67Cu33 cutouts for scanning transmission electron microscopy energy dispersive spectroscopy (STEM-EDS) analysis. Composition mapping was focused on individual Fe and Cu grains to gauge their original non-equilibrium partitioned compositions. STEM-EDS was done on a Thermo Fisher Talos F200X G2 using a low background beryllium double-tilt holder. Figure 5 shows the STEM-EDS maps of the Fe55Cu45 sample and reports a solute concentration of about 12 at.% Cu in the Fe grains and roughly 4 at.% Fe in the Cu grains. STEM-EDS of the Fe67Cu33 sample in Figure 6 reports nearly identical solute concentrations of about 12 at.% Cu in the Fe grains and roughly 4 at.% Fe in the Cu grains. It is important to note that these STEM-EDS results can only be considered semi-quantitative and will serve as a close approximation when compared with our model.

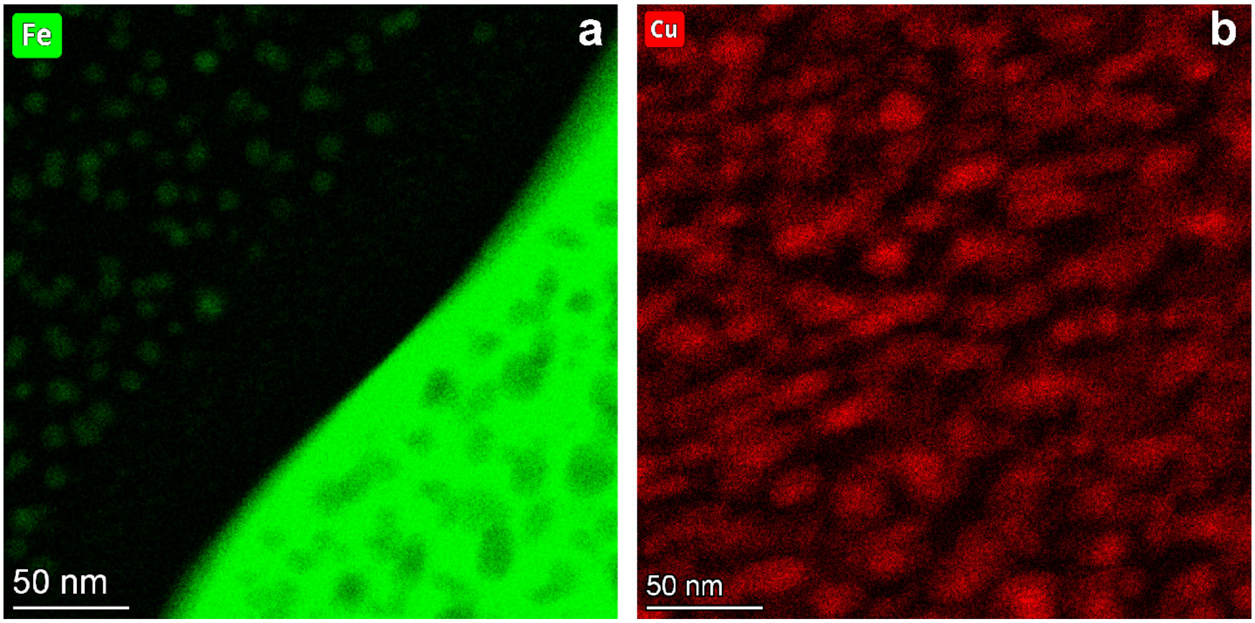

Figure 5. (a) STEM-EDS map of a Cu grain from a Fe55Cu45 sample lift out with Fe nanoprecipitates uniformly dispersed. **(b)** STEM-EDS map of an Fe grain from the same lift out. Numerous larger Cu nanoprecipitates with a slightly oval shape are visible

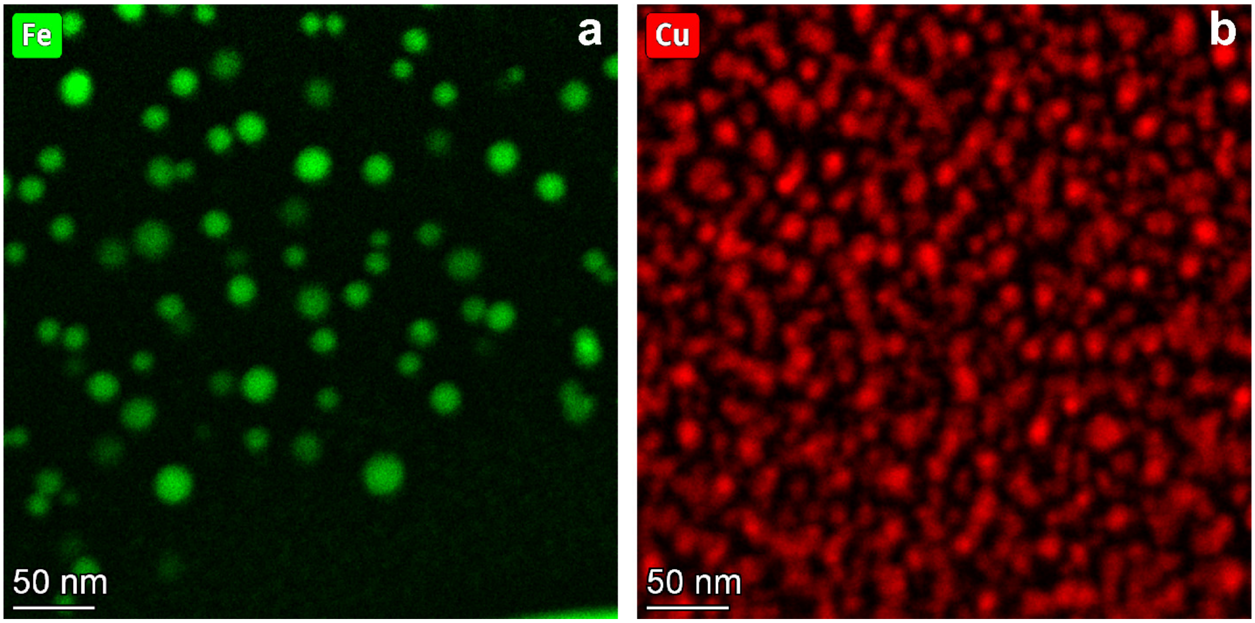

Figure 6. (a) STEM-EDS map of a Cu grain from a Fe67Cu33 sample lift out with Fe nanoprecipitates uniformly dispersed. Note the presence of some large precipitates compared to the smaller ones faintly visible in the background. **(b)** STEM-EDS map of an Fe grain from the same lift out. Precipitates have relatively uniform sizes.

Coincidentally, the solute concentrations of Cu in the Fe grains and Fe in the Cu grains are very similar between the two samples despite the different DED-LB processing parameters used. Compared to the equilibrium solubility limits at the γ(fcc)-Fe + Liquid two-phase region peritectic at 1367 K, the iron grains have roughly twice the equilibrium amount of Cu solute retained within the grain. However, the Cu grains have Fe solute concentrations close to or below the equilibrium amount. In both cases, the lattice of each grain is mostly devoid of solute, indicative that almost all partitioned solute has precipitated out. This is expected as DED-LB builds layer by layer with subsequent layers reheating and partially remelting previously deposited tracks. However, the fine columnar and dendritic grain structures seen in Figure 7 indicates that the reheating duration is not on a timescale long enough to coarsen the grains nor allow for significant macro segregation of phases. Additionally,

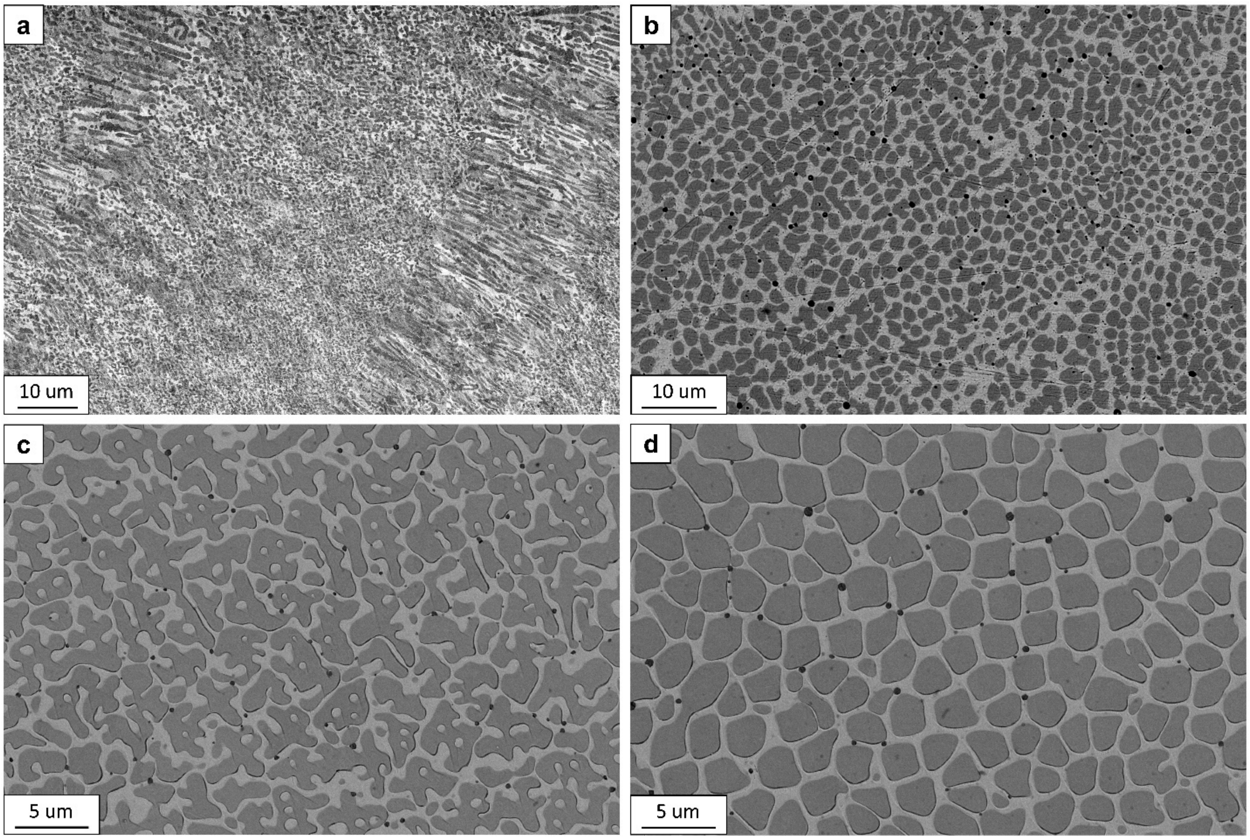

Figure 7. (a) Secondary electron (SE) image and **(b)** Backscattered electron (BSE) image from the Fe55Cu45 sample. Z contrast is such that the Cu phase is lighter and the Fe phase is darker. The orientation for both is perpendicular to the beam scan direction in a top-down view. (a) is just below the free surface and individual tracks are visible oriented diagonally from the bottom left towards the top right. (b) is from the middle of the deposit focused on an overlap region between two tracks. The grain structure is mostly cellular with some dendritic grains. **(c-d)** BSE images from the Fe67Cu33 sample. The orientation is parallel and in the beam scan direction for both. The grain structure is dendritic in (c) and cellular in (d).

3.3) Comparison of Model vs. Experiment

There are deviations between our model and the characterized phase compositions of the DED-LB made samples. The deviation is more severe with the simulated non-equilibrium ε(fcc)-Cu phase when compared with the corresponding STEM-EDS measured Fe solute concentrations in the Cu grains for both the Fe55Cu45 and Fe67Cu33 samples. In both samples, the STEM-EDS measured Fe solute in the Cu grains was at or below the solubility limit for the γ(fcc)-Fe + Liquid two-phase region at the peritectic invariant reaction of 1367 K (5 at.% Fe solute in ε(fcc)-Cu [1]). However, the measured Fe solute concentration in the form of precipitates is still larger than the negligible solubility predicted by the Cu-Fe equilibrium phase diagram at room temperature.

Meanwhile, the simulated non-equilibrium α(bcc)-Fe phase compositions have better agreement with the measured Cu solute concentrations in the Fe grains. This seems to indicate the difference in cooling rate through the γ(fcc)-Fe + Liquid two-phase region between the Fe55Cu45 and Fe67Cu33 samples was not large enough to yield a difference. Indeed, Munitz [2] reported that cooling rates above 10^4 K/s and/or undercoolings greater than 100 K are needed to achieve liquid-liquid phase separation from cooling the homogenous liquid past the spinodal decomposition curve. In such cases, the microstructure of concentrated Cu-Fe alloys transforms from a mainly cellular/dendritic structure to one containing Fe-rich spherulites. The lack of such a microstructure in our DED-LB printed samples indicates that our cooling rate did not yield an undercooling needed to induce the spinodal decomposition. Thus, we can conclude that our samples' solidification followed the normal solidus and liquidus curves and cannot approach the higher solubilities achievable from the liquid-liquid phase separation solidification pathway. Indeed, our Fe55Cu45 STEM-EDS measured solute concentrations have good agreement with those of the undercooled Fe50Cu50 droplets by Luo *et al.* [31] at the smallest undercooling of 20 K.

Subsequently, Munitz [2] mentions that the ability to achieve his reported upper limit of 32.1 at.% Cu solute concentration in the Fe-rich phase is dependent on first achieving the liquid-liquid separation. This limit is supported by Turchanin & Agraval [5] who created a CALPHAD based thermodynamic model of the Cu-Fe phase diagram and showed that the intersection of the T_0 curve with the spinodal decomposition curve denotes the thermodynamic solubility limits of the partitionless crystalline solidified γ(fcc)-Fe and ε(fcc)-Cu phases. Those limits are unbalanced at 34.4 at.% Cu solute in the γ(fcc)-Fe phase while only being 15.7 at.% Fe in the ε(fcc)-Cu phase.

While the non-equilibrium solidus compositions of the Fe55Cu45 and Fe67Cu33 predicted by our model don't differ significantly from the STEM-EDS measured Cu solute concentrations in the α(fcc)-Fe, this is slightly deceptive. The source of the deviation comes from Eq. (20) which is used in conjunction with Eq. (19) to solve for a unique set of non-equilibrium solidus and liquidus compositions. Since the non-equilibrium solidus and liquidus compositions are two independent variables, a second equation is a necessary condition to achieve a unique solution. Eq. (20) accounts for mass conservation and is a reasonable choice given that the overall composition is solved and known for every timestep. The phase fractions in Eq. (20) are defined in Eq. (23)-(24) and are scaled using the same dimensionless solidification term β that shows up in the partitioning Eq. (19). Under equilibrium cooling conditions where $\beta = 0$, the equation simplifies to the lever rule interpretation of the equilibrium phase diagram. Under rapid solidification where $\beta \gg 0$, the phase fractions of the current timestep do not change significantly from the prior timestep with a comparable effect on the non-equilibrium phase compositions.

However, Eq. (23)-(24) include the equilibrium phase fractions $\left(f_{s_{eq}}, f_{s_{eq}}\right)$ and this imposes a constraint that the non-equilibrium phase fractions will scale proportionally to the equilibrium phase fractions as they evolve with temperature within the γ(fcc)-Fe + Liquid two-phase region. This is untrue as the experimentally measured Fe-rich phase in both the Fe55Cu45 and Fe67Cu33 samples have phase fraction values larger than equilibrium.

For the Fe55Cu45 case, the WDS measured overall composition is 45 at.% Cu and the STEM-EDS measured Fe-rich and Cu-rich phase compositions are roughly 12 at.% Cu and 96 at.% Cu respectively. Lever rule calculation yields phase fractions at 0.607 and 0.393 for the Fe-rich and Cu-rich phases respectively. Measuring the phase fraction using ImageJ thresholding of BSE images of the polished Fe55Cu45 sample gives very similar results of roughly 0.622 and 0.378 for the α(bcc)-Fe and ε(fcc)-Cu phases respectively. Meanwhile, our model predicts non-equilibrium solidus and liquidus compositions of 14.9 at.% Cu and 83.5 at.% Cu respectively for nodes with an overall composition of 45 at.% Cu. Lever rule calculation using these compositions yields phase fractions of 0.56 and 0.44 for the Fe-rich and Cu-rich phases respectively. If we take the same overall composition but use the equilibrium solidus and liquidus compositions of the γ(fcc)-Fe + Liquid two-phase region at 6 at.% Cu and 96.1 at.% Cu respectively, we find the phase fractions are 0.567 and 0.433. It should be clear now that our predicted non-equilibrium phase compositions are strongly influenced by the choice of the second equation and our choice of Eq. (20) being proportional to the equilibrium phase fractions persists in the predicted non-equilibrium phase compositions.

We have similar behavior the Fe67Cu33 case, where the model predicts non-equilibrium solidus and liquidus compositions are 14.0 at.% Cu and 78.0 at.% Cu respectively. Lever rule calculation with an overall composition of 33 at.% Cu yields phase fractions at 0.7 and 0.3 for the Fe-rich and Cu-rich phases respectively. These values match the lever rule calculated equilibrium phase fractions almost exactly. Meanwhile, the ImageJ measured phase fractions of the Fe67Cu33 sample are 0.744 and 0.256 for the α(bcc)-Fe and ε(fcc)-Cu phases respectively. Applying the lever rule to the STEM-EDS measured phase compositions and using the WDS measured overall composition of 33 at.% Cu gives 0.75 and 0.25 for the α(bcc)-Fe and ε(fcc)-Cu phase fractions respectively.

3.4) Dendrite Growth Model and Continuous Growth Model

In general, prior work by Lu *et al.*, Luo *et al.*, and Xia *et al.* [4,31,32] utilized the more established continuous growth non-equilibrium partitioning model (CGM) by Aziz [19] which is a concise relationship [Eq. (58)] involving the equilibrium partition coefficient k_{eq}, the solidification front velocity V and a characteristic velocity V_D.

$$k_{ne_{CGM}} = \frac{k_{eq} + \frac{V}{V_D}}{1 + \frac{V}{V_D}} \tag{58}$$

Like our model, Aziz's CGM necessitates a second equation to define a unique set of solidus and liquidus phase compositions. Otherwise, there are infinitely many sets of solidus and liquidus phase compositions that may satisfy a given value of k_{ne}. The aforementioned prior work chose to utilize an Ivantsov function relationship for solute concentration at the dendrite tip as the second equation [Eq. (59)] to define one of the phase compositions at the solid/liquid interface. This Ivantsov function appears in dendrite growth models such as the Lipton-Kurz-Trivedi (LKT) model [Eqs. (62)-(63)] [33, 34].

$$\frac{C_{l_{ne}}}{C_{overall}} = \frac{1}{1-(1-k_{ne})\mathrm{Iv}(Pc_s)} \tag{59}$$

$$\mathrm{Iv}(Pc_s) = Pc_s \exp(Pc_s)\, \mathrm{E}_1\left(\sqrt{Pc_s}\right) \tag{60}$$

$$Pc_s = \frac{vR_{dendrite}}{2D_l} \tag{61}$$

The Ivantsov function itself depends on the solute Peclet number Pc_s which varies depending on the growth velocity and dendrite tip radius. A solution to the Ivantsov function representing the parabolic needle geometry is given [Eq. (60)] and used as this closely matches the microstructure morphology we observe. Other solutions to the Ivantsov function exist and can be derived from a general integral form [34].

As both growth velocity and tip radius are generally unknown and dependent on each other, they are solved as a system of equations [Eqs. (62)-(63)]. The first Eq. (62) is a relationship between the dendrite tip undercooling and its respective components from left to right: non-equilibrium solute effect undercooling, constitutional undercooling, curvature undercooling, and kinetic undercooling. The lack of thermal undercooling is because we are utilizing the directional growth model where the latent heat of solidification is dissipated into the already solidified material.

$$\Delta T_{tip} = \frac{k_{ne}\Delta T_0^V}{1-(1-k_{ne})\mathrm{Iv}(Pc_s)} + (m - m_{ne})C_{overall} + \frac{2\Gamma}{R_{dendrite}} + \frac{V}{\mu_k} \tag{62}$$

$$V\left(\frac{k_{ne}\Delta T_0^V}{D_l}\right)\left(\frac{1}{1-(1-k_{ne})\mathrm{Iv}(Pc_s)}\right)\left(1 - \frac{2k_{eq}}{\sqrt{1+\frac{1}{\sigma^* {Pc_s}^2}} - 1 + k_{ne}}\right) - G = \frac{2\Gamma}{\sigma^* {R_{dendrite}}^2} \tag{63}$$

The second equation Eq. (63) represents the dendrite tip radius selection. Here, we relate the growth velocity to the radius via a selection criteria parameter σ^*. State-of-the-art work leans heavily on the micro-solvability theory which considers the anisotropic surface tension at the dendrite tip. However, applying the micro-solvability theory for the selection criteria parameter in three dimensions is difficult as the anisotropy is often determined experimentally. Therefore, when the interface anisotropy is unknown, the marginal stability criterion is used which assumes that there is negligible anisotropy at the tip. This reduces the selection criteria parameter to a constant value around 0.025 or $\frac{1}{4\pi^2}$. While this will introduce some error when applied to material systems where there is non-negligible anisotropy, the deviation from theory to experiment is usually less than 1 order of magnitude as examined by Lu & Hunt [35]. Thus, with the two equations we have three unknowns ($\Delta T_{tip}, V, R_{dendrite}$) of which one is needed *a priori* to solve.

3.5) Application of Dendrite Growth Model to DED-LB:

Prior work by Lu *et al.* and Luo *et al.* [4,31] focused on small droplets of Cu-Fe alloys where the bulk undercooling could be measured from the temperature spike indicating recalescence. This eliminates one of the unknowns and allowed the authors to solve the system of equations [Eqs. (62)-(63)]. In DED-LB it is not possible to measure a single recalescence point as solidification is a continuous process with a solid/liquid interface that follows the laser-powder nozzle. However, with a couple assumptions, it is possible to utilize just Eq. (63) to solve for the Ivantsov function value and calculate non-equilibrium phase compositions.

1. We assume that directional growth is the primary mode of solidification and neglect the contribution of equiaxed grains homogeneously nucleated from the melt pool.
2. The directional dendrite growth velocity is assumed to directly related to the melt pool interface velocity via the angle of interface normal vector off the laser scanning direction.

The first assumption is valid for most of the melt pool volume as partially remelted grains of the substrate or prior deposited layer serve as heterogenous nucleation points for directional solidification. Homogenous solidification requires a higher driving force for nucleation and is likely only near the free surface where the cooling rate is highest. Heterogenous nucleation is expected as most additively manufactured alloys display anisotropic mechanical properties from grains oriented in the laser scanning direction of each track.

The second assumption [Eq. (64)] subsequently falls into place based on the principle defined by the first. Once a melt pool interface has developed, it will eventually stabilize into a parabolic ellipsoid shape that trails the laser focal point scanning across the surface. Dendrites will grow normal to this melt pool interface as the melt pool interface is matched by a temperature gradient. The dendrites' growth velocity V can be calculated as the product of the laser scan velocity V_{beam} and the cosine of the normal angle to the interface θ_{sl}. In laser additive processes, the energy input is small relative to the large substrate minimizing heat accumulation. Therefore, at steady state the melt pool interface will trail the laser focal point by a constant distance such that in the laser's reference frame, the melt pool interface location will be constant.

The second assumption itself is also dependent on the melt pool interface shape remaining consistent. This relies on the correct choice of laser power and scan speed from 2D process maps and falls apart at the two extremes. The first is where the laser power is very high, and the scanning speed is very low while the second is the inverse of the former. In the first extreme, high laser power leads to keyholing and the formation of trapped pores due to instability near the bottom of the sharp melt-pool. In the second, fast scan speed leads to balling where the shallow melt-pool is unstable and pinches off frequently due to surface tension effects. For the purpose of calculating non-equilibrium phase compositions, we consider that an appropriate choice of laser scan speed (and laser power) is implied with the second assumption.

$$V = V_{beam}\cos(\theta_{sl}) \tag{64}$$

Eq. (65) is a rearrangement of Eq. (63) where $R_{dendrite}$ is eliminated using the relationship established by the solute Peclet number [Eq. (61)]. Since the growth velocity is known from Eq. (64), the solute Peclet number can be solved in Eq. (65) and then utilized in Eq. (59) to solve for the non-equilibrium phase compositions. As the Ivantsov function contains the exponential integral and Eq. (65) does not simplify well, Newton's method is used to solve for Pc_s.

$$\frac{\Gamma V^2}{4\sigma^* Pc_s {D_l}^2} - \frac{V}{D}\left(1 - \frac{2k_{eq}}{\sqrt{1 + \frac{1}{\sigma^* {Pc_s}^2}} - 1 + k_{ne}}\right)\left(\frac{k_{ne}\Delta T_0^V}{1 - (1 - k_{ne})\mathrm{Iv}(Pc_s)}\right) + G = 0 \tag{65}$$

3.6) Source of Deviations: Models vs. Experiment

Unfortunately, a direct implementation of the LKT model does not match well to experimental results of rapidly solidified concentrated Cu-Fe alloys. Therefore, neither solving Eqs. (62)-(63) nor Eq. (65) followed by Eq. (59) will yield appropriate non-equilibrium phase compositions. Luo *et al.* [31] reported their measured growth velocities of undercooled 50Cu50Fe alloys were much greater than those calculated using the LKT model for all measured undercoolings ranging from 20 K to 261 K below their selected equilibrium liquidus temperature of 1711 K.

We identify the likely cause to be the characteristic velocity V_D used to solve for $k_{ne_{CGM}}$ in Eq. (58). This parameter should be fit to experimental data which normally precludes the use of this model for material systems with little data. In cases where experimental data is unknown *a priori*, many authors tend to define the characteristic velocity as a diffusive velocity [Eq. (66)] where D_l is the liquid interdiffusion coefficient and a_0 is the characteristic diffusion length.

$$V_D = \frac{D_l}{a_0} \tag{66}$$

This implementation leads to a relatively constant V_D as while D_l varies with temperature, it does not change significantly in order of magnitude. As such, we would normally expect the growth velocity to reach and exceed V_D at some undercooling which dictates the beginning of partitionless solidification at $V = V_D$. This definition is a slight modification of Aziz's CGM by Sobolev [36] as for large values of k_{eq}, $k_{ne_{CGM}}$ would normally not approach 1 until $V \gg V_D$, contrary to experiment.

In Figure 8(a), we observe that the calculated $V_{D_{Luo}}$ [Eq. (68)-(69)] is not constant with undercooling and has a curvature similar to the experimentally measured V_{Luo}. This is contrary to the previously defined method for calculating V_D as a diffusive velocity. Since the liquid diffusion coefficient D_l does not change significantly with temperature, V_D would appear as a relatively flat line in Figure 8(a) showcasing low undercooling sensitivity.

$$V_{Luo} = 6.47 * 10^{-5} \Delta T^{2.22} \tag{67}$$

$$V_{D_{Luo}} = \frac{V_{Luo}\left(k_{ne_{Luo}} - 1\right)}{k_{eq} - k_{ne_{Luo}}} \tag{68}$$

$$V_{D_{Luo}} = 4 * 10^{-14} \Delta T^{6} - 5 * 10^{-11} \Delta T^{5} + 3 * 10^{-8} \Delta T^{4} - 9 * 10^{-6} \Delta \mathrm{T}^{3} + 0.0018 \Delta T^{2} - 0.005 \Delta T + 0.0099 \tag{69}$$

Consequently, since V_{Luo} approaches $V_{D_{Luo}}$ very slowly, $k_{ne_{CGM}}$ will not go to 1 which indicates that fully partitionless solidification is out of reach for concentrated Cu-Fe alloys. Indeed, in Figure (8)b, the plotted non-equilibrium partition coefficient curve is relatively linear which is contrary to normal k_{ne} curves that approach 1 with an error function like shape. This behavior differs from dilute Cu-Fe alloys with low Cu concentrations that lie within the δ(bcc)-Fe + Liquid two phase region. For those dilute Cu-Fe alloys, Xia *et al.* [32] showed that fully partitionless solidification was achievable in highly undercooled droplets solidified in a manner identical to the experiments done by Luo *et al.* [31]. Nevertheless, the key issue is that for $k_{ne_{CGM}}$ to match $k_{ne_{Luo}}$, V_D cannot be relatively constant in magnitude as predicted by Eq. (66) and which was used by Luo *et al.* [31]. Therefore, the $k_{ne_{CGM}}$ which they calculated and used for solving the LKT model [Eqs. (62)-(63)] would not yield the correct growth velocity V as they showed, nor correctly predict the non-equilibrium phase compositions [Eq. (59)].

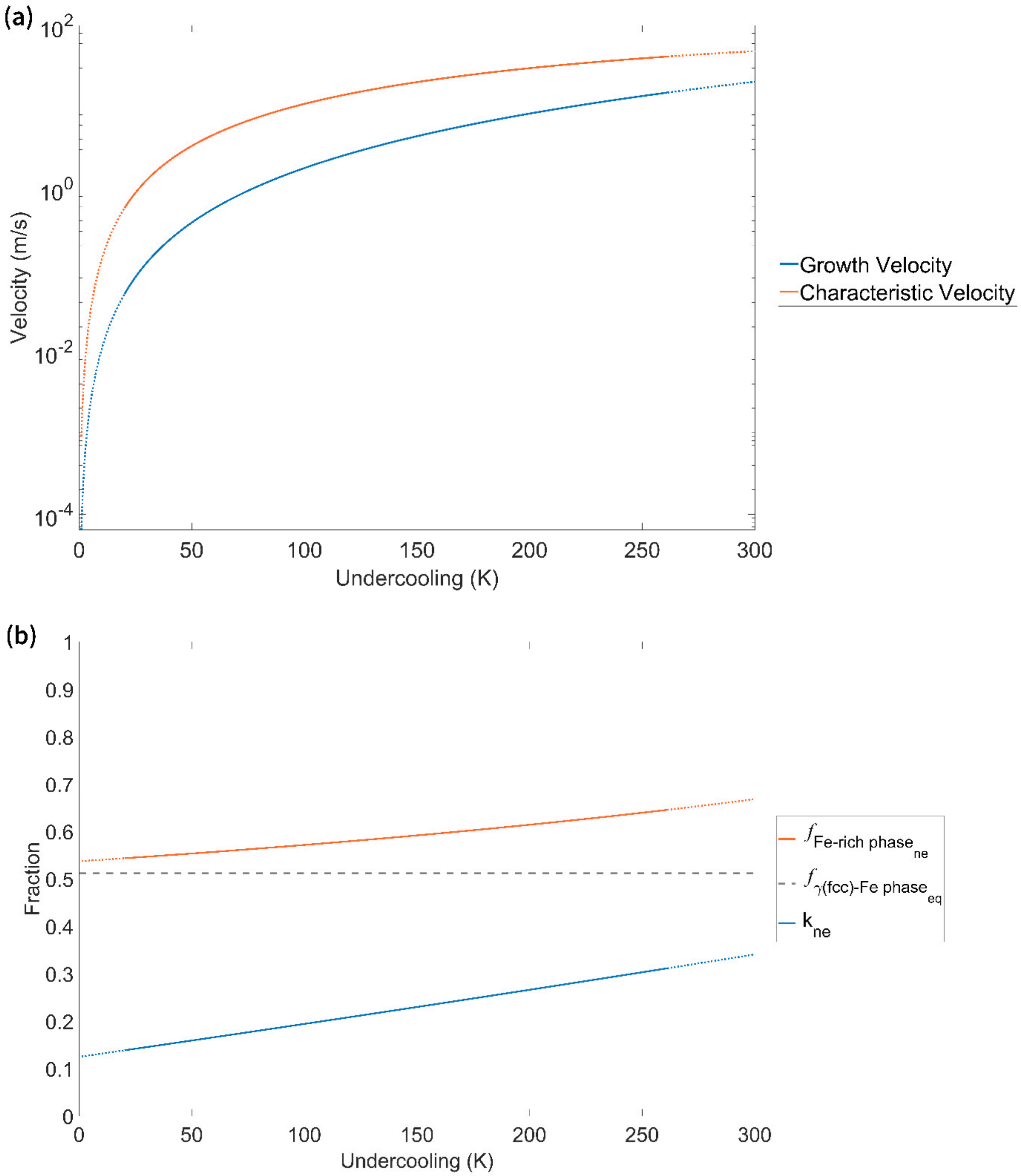

Figure 8. (a) Comparison of fit equation of growth velocity V_{Luo} from multiple experimental measurements by Luo *et al*. [31] against back-calculated characteristic velocity $V_{D_{Luo}}$. The solid lines represent the range of undercoolings (20 K – 261 K) achieved in experiment while the dotted portions are extrapolated. **(b)** Fit equations of non-equilibrium partition coefficient k_{ne} and the Fe-rich phase fraction from experiment by Luo *et al.* [31]. The range of undercoolings (20 K – 261 K) is represented by solid lines while the dotted extensions are extrapolated. The horizontal grey line represents the equilibrium phase fraction of the γ(fcc)-Fe phase at the peritectic isotherm of 1367 K located on the bottom of the γ(fcc)-Fe + Liquid two phase region in the Cu-Fe equilibrium phase diagram. Its extension across the undercooling range is merely for visual comparison against the non-equilibrium Fe-rich phase fraction that increases with higher undercooling.

Additionally, Luo *et al.* [31] experimentally measured the degree of phase separation at various undercoolings and measured the solute concentrations within the Fe-rich and Cu-rich phases that formed post Liquid-Liquid spinodal decomposition. With those data points, we plot Figure 8(b) to show an approximate comparison of experimental Fe-rich phase fraction against the equilibrium value used in our model [Eq. (20)]. The plotted Fe-rich phase fraction curve represents the lower bound as it is calculated using the lever rule with an overall composition of 50 at.% Cu. The actual measured overall composition of the Fe-rich phase decreases with increasing undercooling which is expected as the spinodal curve widens at lower temperatures. The lower bound is used as the measured bulk Cu concentrations of the Fe-rich zone in droplets solidified at higher undercoolings are less than their corresponding Cu solute concentrations in just the Fe-rich phase [31].

We can see that the plotted phase fraction increases with higher undercoolings which corresponds with higher degrees of non-equilibrium partitioning. This is in line with our findings where our ImageJ measured Fe-rich phase fraction was slightly higher than equilibrium for both the Fe55Cu45 and Fe67Cu33 samples. Thus, we confirm our earlier analysis that another choice of the second equation to complete our model is needed as the non-equilibrium phase fractions are also variable with solidification velocity/undercooling.

4) Summary and Conclusions:

A comprehensive transport and laser powder interaction model was developed to accurately simulate the DED-LB process. The computed thermal and composition history from the transport model was then used to solve a non-equilibrium partitioning model predicting the non-equilibrium phase compositions that form in rapidly solidified concentrated Cu-Fe alloys.

The non-equilibrium phase compositions of the Fe55Cu45 and Fe67Cu33 alloys are very similar despite different processing parameters and very different mechanical behavior. The α(bcc)-Fe phases contained around 12 at.% Cu solute and the ε(fcc)-Cu phases had roughly 4 at.% Fe solute. Yet Chatterjee *et al.* [7] showed that the Fe55Cu45 alloy has twice the compressive yield but far less strain hardening compared to the Fe67Cu33 alloy. Therefore, just predicting initial trapped solute concentration is not sufficient to deriving a correlation to mechanical properties of the resulting alloy. Indeed, the authors [7] found that both the precipitate area fraction as well as type of precipitates (coherent, incoherent) played a role in strengthening the alloys above their theoretical Hall-Petch predicted strength.

There is deviation in the predicted non-equilibrium phase compositions of our model compared to the STEM-EDS measured samples. The model generally predicts more non-equilibrium partitioning and higher solute concentrations in both the α(bcc)-Fe and ε(fcc)-Cu phases. The deviation is more severe with the predicted non-equilibrium liquidus compositions which represent the Fe solute concentration in the ε(fcc)-Cu phase at up to 20 at.% Fe greater than measured. Meanwhile the deviation is very minor for the predicted non-equilibrium solidus compositions at only 2.9 at.% Cu and 2.3 at.% Cu greater than measured for the Fe55Cu45 and Fe67Cu33 cases respectively. The difference in deviation between the non-equilibrium solidus and liquidus compositions is due to the higher phase fraction of α(bcc)-Fe which amplifies small inaccuracies of the non-equilibrium solidus.

When compared against prior work on undercooled concentrated Cu-Fe alloys [4, 31], our DED-LB made samples produce non-equilibrium phase compositions that would fall within the 5 K to 10 K undercooling range. These undercoolings lie above the spinodal decomposition curve which is correlated by the lack of Fe spherulite in the microstructure that indicate the occurrence of a Liquid-Liquid separation. Our microstructure is a mix of cellular and dendritic grains indicating that localized solidification velocities fall within the cellular-dendritic transformation region.

We identify the characteristic velocity V_D as being the key deficiency in utilizing the Aziz CGM for concentrated Cu-Fe alloys. Prior work has often utilized the Aziz CGM alongside the LKT dendrite growth model [37, 38, 39] to account for the non-equilibrium effects. And indeed, in dilute alloys and for material systems where V_D may be fit to experimental data the CGM does work well. Similarly, we identify the deficiency in our non-equilibrium partitioning model as the second Eq. (20) which assumed non-equilibrium phase fractions were proportional to their equilibrium counterparts. This was proven false, and those phase fractions deviate from equilibrium dependent on the undercooling.

Modeling non-equilibrium partitioning in concentrated Cu-Fe alloys will require additional research as neither the Aziz CGM with LKT model nor our model can account for the unique behavior of the spinodal curve that extends deep into the γ(fcc)-Fe + Liquid two phase region. This is despite the former model showing good agreement when compared against rapidly solidified dilute Cu-Fe alloys that fall solely in the δ(bcc)-Fe + Liquid two phase region [32].

Acknowledgements

This work was supported by the Department of Energy, National Nuclear Security Administration under Award no. DE-NA0003857.

The authors acknowledge the financial support of the University of Michigan College of Engineering and technical support from the Michigan Center for Materials Characterization (MC^2).

The authors would like to thank the staff at the University of Michigan School of Earth and Environmental Sciences, Robert B. Mitchel Electron Microbeam Analysis Lab (EMAL) for their support in the wavelength dispersive spectroscopy material characterization.

Data Statement

Simulation data and post-processed data may be made available on request. Please send requests to the corresponding author.

Simulation code may be made available on request. Please send requests to the corresponding author.

References:

[1] Turchanin, M., Agraval, P., MSIT, Effenberg, G. (ed.) *Cu-Fe Binary Phase Diagram Evaluation*. 20.11107.1.5, Materials Science International Services GmbH, Stuttgart, (2014) https://materials.springer.com/msi/docs/sm_msi_r_20_011107_01

[2] Munitz, A. *Liquid separation effects in Fe−Cu alloys solidified under different cooling rates*. Metall Mater Trans B 18, 565–575 (1987). https://doi.org/10.1007/BF02654269

[3] Liu, S.C., Jie, J.C., Guo, Z.K., Yin, G.M., Wang, T.M., Li, T.J. *Solidification microstructure evolution and its corresponding mechanism of metastable immiscible Cu80Fe20 alloy with different cooling conditions.* Journal of Alloys and Compounds 742(25), 99-106 (2018). https://doi.org/10.1016/j.jallcom.2018.01.306

[4] Lu, X.Y., Cao, C.D., Wei, B. *Microstructure evolution of undercooled iron-copper hypoperitectic alloy*. Materials Science and Engineering: A 313(1-2), 198-206 (2001). https://doi.org/10.1016/S0921-5093(01)00928-5

[5] M.A. Turchanin, P.G. Agraval, *Thermodynamics of Liquid Alloys, and Stable and Metastable phase Equilibria in the Copper-Iron System*. Powder Metallurgy and Metal Ceramics: 40, 307-319 (2001). https://doi.org/10.1023/A:1013825102788

[6] Cui, W.C., Wang, L., Peng, C.X., Song, K.K. *Phase separation and structure transition of undercooled Fe75Cu25 melts*. Physics and Chemistry of Liquids 56(3), 290-298 (2017). https://doi.org/10.1080/00319104.2017.1327583

[7] A. Chatterjee, E. Sprague, J. Mazumder, A. Misra, *Hierarchical microstructures and deformation behavior of laser direct metal deposited Cu-Fe alloys*, Materials Science and Engineering: A 802, 140659 (2021). https://doi.org/10.1016/j.msea.2020.140659

[8] Zafari, A., Xia, K. *Laser powder bed fusion of ultrahigh strength Fe-Cu alloys using elemental powders.* Additive Manufacturing 47, (2021). https://doi.org/10.1016/j.addma.2021.102270

[9] Zafari, A., Xia, K. *Nano/ultrafine grained immiscible Fe-Cu alloy with ultrahigh strength produced by selective laser melting*. Materials Research Letters 9(6), 247-254 (2021). https://doi.org/10.1080/21663831.2021.1884620

[10] He, X.; Song, L.; Yu, G.; Mazumder, J. *Solute Transport and Composition Profile during Direct Metal Deposition with Coaxial Powder Injection*. Appl. Surf. Sci. 258(2), 898–907 (2011). https://doi.org/10.1016/j.apsusc.2011.09.023

[11] Qi, H.; Mazumder, J.; Ki, H. *Numerical Simulation of Heat Transfer and Fluid Flow in Coaxial Laser Cladding Process for Direct Metal Deposition*. J. Appl. Phys. 100(2), 024903 (2006). https://doi.org/10.1063/1.2209807

[12] Wu, J.Z., Wei, H.Y., Yuan, F.B., Zhao, P.H., Zhang, Y. *Effect of beam profile on heat and mass transfer in filler powder laser welding*. Journal of Materials Processing Technology 258, 47-57 (2018). https://doi.org/10.1016/j.jmatprotec.2018.03.011

[13] Wu, J.Z., Zhao, P.H., Wei, H.Y., Lin, Q.D., Zhang, Y. *Development of powder distribution model of discontinuous coaxial powder stream in laser direct metal deposition*. Powder Technology 340, 449-458 (2018). https://doi.org/10.1016/j.powtec.2018.09.032

[14] Lin, J. *Laser attenuation of the focused powder streams in coaxial laser cladding*. Journal of Laser Applications, 12(1), 28-33 (2000). https://doi.org/10.2351/1.521910

[15] Pinkerton, A. J. *An analytical model of beam attenuation and powder heating during coaxial laser direct metal deposition*. Journal of Physics D: Applied Physics, 40(23), 7323-7334 (2007). https://doi.org/10.1088/0022-3727/40/23/012

[16] Pinkerton, A. J. Li, L. *Modelling Powder Concentration Distribution from a Coaxial Deposition Nozzle for Laser-Based Rapid Tooling*. Journal of Manufacturing Science and Engineering, 126(1), 33-41 (2004). https://doi.org/10.1115/1.1643748

[17] Wang, J., Han, F., Chen, S., & Ying, W. *A novel model of laser energy attenuation by powder particles for laser solid forming*. International Journal of Machine Tools and Manufacture 145, 103440 (2019). https://doi.org/10.1016/j.ijmachtools.2019.103440

[18] Yin, D., Misra, A. & Mazumder, J. *Modeling of non-equilibrium partitioning in direct metal deposited copper–iron concentrated alloys*. Journal of Materials Research 37, 705-718 (2022). https://doi.org/10.1557/s43578-022-00487-4

[19] Aziz, M.J. *Model for solute redistribution during rapid solidification*. J. Appl. Phys. 53(2), 1158-1168 (1982). https://doi.org/10.1063/1.329867

[20] Gurtin, M.E. *On the two-phase Stefan problem with interfacial energy and entropy*. Arch. Rational Mech. Anal. 96, 199-241 (1986). https://doi.org/10.1007/BF00251907

[21] Asai, S., Muchi, I. *Theoretical analysis and model experiments on the formation mechanism of channel-type segregation*, Trans. Iron Steel Inst. Jpn. 18, 90–98 (1978). https://doi.org/10.2355/isijinternational1966.18.90

[22] F. Seitz, *The Modern Theory of Solids*, McGraw-Hill, New York, USA, (1940)

[23] Chase, M.W., Jr. *NIST-JANAF Themochemical Tables, Fourth Edition*, J. Phys. Chem. Ref. Data, Monograph 9, 1-1951 (1998).

[24] Powell, R.W., Ho, C.Y., Liley, P.E. *Thermal Conductivity of Selected Materials*, National Standard Reference Data Series – National Bureau of Standards – 8, West Lafayette, 13-35 (1966).

[25] Kar, A.; Mazumder, J. *Model for nonequilibrium partitioning during rapid solidification of binary concentrated solutions*, Acta Metallurgica et Materialia. 40(8), 1873-1881 (1992). https://doi.org/10.1016/0956-7151(92)90174-D

[26] R. van-Engelen, *Improving the Double Exponential Quadrature Tanh-Sinh, Sinh-Sinh and Exp-Sinh Formulas*, https://www.genivia.com/qthsh.html, 2022 (accessed 14 September 2022).

[27] C.Y. Liu, J. Lin, *Thermal processes of a powder particle in coaxial laser cladding*, Opt. Laser Technol., 35, 81-86 (2003). https://doi.org/10.1016/S0030-3992(02)00145-7

[28] Gan, Z., Yu, G., He, X., Li, S. *Numerical simulation of thermal behavior and multicomponent mass transfer in direct laser deposition of Co-base alloy on steel*. Int. J. Heat Mass Tran. 104, 28-38 (2017). https://doi.org/10.1016/j.ijheatmasstransfer.2016.08.049

[29] I. Gibson, D. Rosen, B. Strucker, *Directed energy deposition process*, Additive manufacturing technology, Berlin: Springer., 245-268, (2015).

[30] Donovan, J.J., Allaz, J.M., Handt, A.V.D., Seward, G.G.E., Neill, O., Goemann, K., Chouinard, J., Carpenter, P.K. *Quantitative WDS compositional mapping using the electron microprobe*, American Mineralogist, 106, 1717-1735 (2021). https://doi.org/10.2138/am-2021-7739

[31] Luo, S.B., Wang, W.L., Chang, J., Xia, Z.C., Wei, B. *A comparative study of dendritic growth within undercooled liquid pure Fe and Fe50Cu50 alloy*. Acta Materialia 69, 355-364 (2014). https://doi.org/10.1016/j.actamat.2013.12.009

[32] Xia, Z.C., Wang, W.L., Luo, S.B., Wei, B. *Specific heat capacity and dendritic growth kinetics of liquid peritectic Fe-Cu alloys*. Chemical Physics Letters 658, 220-223 (2016). https://doi.org/10.1016/j.cplett.2016.06.059

[33] J. Lipton, W. Kurz, R. Trivedi, *Rapid dendrite growth in undercooled alloys.* Acta Metallurgica, 35(4), 957-964 (1987). https://doi.org/10.1016/0001-6160(87)90174-X

[34] R. Trivedi, W. Kurz, *Dendritic growth*. International Materials Reviews, 39(2), 49-74 (1994). https://doi.org/10.1179/imr.1994.39.2.49

[35] S.Z. Lu, J.D. Hunt, *A numerical analysis of dendritic and cellular array growth: the spacing adjustment mechanisms*, Journal of Crystal Growth, 123(1-2), 17-34 (1992). https://doi.org/10.1016/0022-0248(92)90006-5

[36] S.L. Sobolev, *Rapid phase transformation under local non-equilibrium diffusion conditions*, Materials Science and Technology, 31(13), 1607-1617 (2015). https://doi.org/10.1179/1743284715Y.0000000051

[37] D.W. Heard, R. Gauvin, M. Brochu, *Non-equilibrium solute partitioning in a laser re-melted Al–Li–Cu alloy*, Acta Materialia, 61(19), 7432-7436 (2013). https://doi-org/10.1016/j.actamat.2013.08.050

[38] Y.L. Xue, S.M. Li, H. Zhong, K.W. Li, H.Z. Fu, *Phase selections and mechanical properties of ternary Cr-Nb-Ti alloys under rapid solidification*, Journal of Alloys and Compounds, 684(5), 403-411 (2016). https://doi.org/10.1016/j.jallcom.2016.05.207

[39] S. Ghosh, L. Ma, N. Ofori-Opoku, J.E. Guyer, *On the primary spacing and microsegregation of cellular dendrites in laser deposited Ni–Nb alloys*, Modelling Simul. Mater. Sci. Eng. 25, 065002 (2017). https://doi.org/10.1088/1361-651X/aa7369